International Journal of Mechanical Sciences 264 (2024) 108819

Contents lists available at ScienceDirect

International Journal of Mechanical Sciences

journal homepage: www.elsevier.com/locate/ijmecsci

Compression behavior of 4D printed metamaterials with various Poisson's ratios

Peilei Xu [a], Xin Lan [b], Chengjun Zeng [a], Xudong Zhang [a], Hanxing Zhao [b], Jinsong Leng [b], Yanju Liu [a,*]

[a] Department of Astronautical Science and Mechanics, Harbin Institute of Technology, Harbin 150001, PR China
[b] Centre for Composite Materials and Structures, Harbin Institute of Technology, Harbin 150080, PR China

ARTICLE INFO

Keywords:
Cellular metamaterials
4D printing
Zero Poisson's ratio
Vibration isolation
Shape memory polymers

ABSTRACT

In this study, three types of cellular metamaterials with negative/zero/positive Poisson's ratio and vibration isolation effects were devised and fabricated based on 4D printing of shape memory polymers. The compressive properties and energy absorption capacity of three cellular metamaterials at variable temperatures were evaluated by finite element simulations and compression experiments. To explore the application possibilities of 4D printed cellular metamaterials in deformable structures, shape recovery experiments were carried out, and the results showed that the three types of cellular metamaterials exhibited a high shape recovery rate. The vibration modes and vibration isolation capabilities of 4D printed cellular metamaterials were investigated for three types of cellular metamaterials with negative/zero/positive Poisson's ratio. In addition, based on the deformation reversible capability of the structure, the vibration isolation capability of three cellular metamaterial structures was investigated under different deformation stages. The results demonstrate that the cellular metamaterials with zero Poisson's ratio possess superior vibration isolation capability compared to negative or positive Poisson's ratio cellular metamaterials at different deformation stages by a comprehensive analysis. The methods and conclusions presented in this study will guide the design of functionalized cellular metamaterials with high energy absorption, strong vibration isolation, and autonomous deformation ability.

1. Introduction

The hexagonal honeycomb structural pattern is frequently encountered in porous materials. Such pattern has been optimized for varied application scenarios, resulting in the production of numerous honeycomb structures featuring diverse topological morphology. According to specific application scenarios, cellular structures have developed from hexagons to quadrangles [1–3], triangles [4–6], and other similar geometric shapes [7–10]. Due to its high stiffness in the out-of-plane direction, low mass and outstanding mechanical properties, honeycomb structures have found widespread use in conventional building design [11,12], various-winged aircraft [13–15], as well as in the nano and biomedical fields [16–19].

Over the years, metamaterial structures have garnered much attention. Several scholars have examined the functionality of diverse cellular structures in varying settings [20–25]. In addition, studies have demonstrated the remarkable attributes of honeycomb metamaterial structures in terms of their resistance to bending [26–30], ability to absorb energy [31–35], and efficacy in resisting impacts [36–40]. The honeycomb structure with its hexagonal shape offers various manufacturing possibilities and allows for the use of different materials. Moreover, it demonstrates favorable properties, such as a positive Poisson's ratio (PPR) and a high value of specific energy absorption [41,42]. As a type of tensile expansion material, the concave hexagonal honeycomb structure exhibits negative Poisson's ratio (NPR) properties. NPR honeycomb metamaterials exhibit favorable shear resistance [43–45] and energy absorption properties [46–48]. Based on the above two structures, Brocolo et al. [49] designed a hybrid honeycomb metamaterial with a zero Poisson's ratio (ZPR). This structure boasts a substantially higher load-bearing capacity and is of particular interest due to the unique ZPR effect [50–54].

However, the honeycomb structures currently in use are constructed with conventional materials and possess fixed properties, making it challenging to adjust to changing mechanical surroundings [55]. By

* Corresponding author.
E-mail address: yj_liu@hit.edu.cn (Y. Liu).

https://doi.org/10.1016/j.ijmecsci.2023.108819
Received 15 July 2023; Received in revised form 18 September 2023; Accepted 10 October 2023
Available online 11 October 2023

incorporating smart materials into 3D printing [56–59], 4D printing enables the creation of metamaterial structures that are mechanically adaptable and capable of active deformation [60–67]. Compared to the traditional 3D printing structure, the 4D printing structure is no longer statically stable. Its morphology and properties change dynamically over time [68,71]. Shape memory polymer (SMP), a frequently employed smart material, has found wide application in 4D printing [68–72]. Structures created through 4D printing are widely used in soft robotics in comparison to alternative manufacturing techniques [35,73-77]. Zolfagharian et al. [35] created muscles using 3D printing that respond to stimulus signals and developed programmable joints capable of displaying different levels of stiffness. They also developed programmed joints able to exhibit varying levels of stiffness. Bodaghi et al. [73] employed a bionic lattice chamber to devise a soft pneumatic actuator (SPAs) that exhibits distinct behaviors for regulating tip deflection and tip force whilst utilizing identical input air pressure. Li et al. (75) employed 4D printing to create soft actuators that possess intrinsic self-awareness feedback and adjustable stiffness. In addition to these applications, extensive research on metamaterials and superstructures in vibration isolation has been explored [78]. Jiang et al. [79] created a mechanical metamaterial that demonstrates excellent energy shielding efficacy within the low-frequency spectrum. Zhang et al. [80] incorporated a negative stiffness magnetic spring into the linear isolator, resulting in improved isolation performance under low-frequency excitation. This improvement was successfully demonstrated.

In this paper, three types of cellular metamaterials were constructed using shape memory polymer (SMP) through 4D printing. Firstly, compression experiments and finite element analyses were conducted on three types of cellular metamaterials at variable temperatures. The mechanical and energy absorption properties of three cellular metamaterials were assessed at variable temperatures, with an evaluation of the distinctions between the three categories of cellular metamaterials. The compression modulus and compression strength evolution curves at variable temperatures were acquired for three cellular metamaterials. Additionally, the vibration isolation capability of three cellular metamaterials was examined under different deformation factors, using a vibration isolation testing system. Exploring the low-frequency vibration isolation characteristics of three cellular metamaterials could offer innovative insights for low-frequency vibration isolation structures.

In this paper, shape memory polymer (SMP) was used to construct three types of cellular metamaterials by 4D printing. Firstly, compression experiments and finite element analyses of three types of cellular metamaterials were carried out at variable temperatures. The mechanical and energy absorption properties of three cellular metamaterials were investigated at variable temperatures, and the differences between the three types of cellular metamaterials were evaluated. The evolution curves of compression modulus and compression strength with temperature for three cellular metamaterials were also obtained. In addition, the vibration isolation ability of three cellular metamaterials under different deformation conditions was studied utilizing a vibration isolation testing system. Exploring the low-frequency vibration isolation characteristics of three cellular metamaterials can provide creative new perspectives for low-frequency vibration isolation structures. Finally, the intelligent recovery process of three types of cellular metamaterials printed using 4D printing was demonstrated through a shape recovery experiment.

2. Materials and methods

In this section, the design methods for three cellular metamaterials were initially explained. The detailed dimensions of the three cellular metamaterials were determined thereafter. Subsequently, the process of printing and fabricating three cellular metamaterials was described, with detailed information about the workflow of the compression test. To determine the printed material's fundamental parameters, standard tensile specimens were utilized for conducting tensile tests. This section describes the modelling and parameterization of the finite element simulation, as well as the behavioral representations of shape memory. Additionally, it outlines the arrangement and principles of the experimental equipment used in the vibration isolation characteristics test.

2.1. Structural design

Hexagonal honeycomb structures are typical examples of PPR multicellular materials. The concave hexagonal honeycomb structure serves as a tensile expansion material and exhibits NPR characteristics. Olympio and Gandhi [81] derived analytical expressions for the mechanical properties of conventional hexagonal honeycomb. As shown in the Fig. 1, the conventional hexagonal positive Poisson's ratio honeycomb under pressure in the Y direction, the Poisson's ratio in the X direction is

$$\nu_{yx} = \frac{\cos^2\theta}{(1+\sin\theta)\sin\theta}\frac{l^2+(K-1)t^2}{l^2+(K+\cot^2\theta)t^2} \tag{1}$$

where K represents the coefficient of arm shear deformation. The typical value for K is $K = 2.4 + 1.5\nu$. ν represents the Poisson's ratio of the structural material.

The conventional hexagonal honeycomb structure exhibits negative Poisson's ratio effect when + θ becomes − θ. On this basis, a ZPR structure with alternating hexagon and concave hexagon elements was designed. When the ZPR structure is pressurized in the Y direction, the deformation of each ZPR cell element unit in the Y direction is $u_y = 2\varepsilon_y(\theta)l\cos\theta = 2\varepsilon_y(-\theta)l\cos\theta$. The overall strain in the Y direction for ZPR structure is

$$\varepsilon_y = \frac{u_y}{2l\cos\theta} = \varepsilon_y(\theta) = \varepsilon_y(-\theta) \tag{2}$$

The overall strain of a ZPR structure in the X direction can be expressed as:

$$\varepsilon_x = \frac{u_x(\theta)+u_x(-\theta)}{4l} = \frac{\varepsilon_x(\theta)(1+\sin\theta)+\varepsilon_x(-\theta)(1-\sin\theta)}{2} \tag{3}$$

Because of $\varepsilon_x = -\nu_{yx}\varepsilon_y$, the Poisson's ratio of the ZPR structure in the X direction can be expressed as:

$$\nu_{yx} = -\frac{\varepsilon_x}{\varepsilon_y} = \frac{\nu_{yx}(\theta)(1+\sin\theta)+\nu_{yx}(-\theta)(1-\sin\theta)}{2} = 0 \tag{4}$$

It can be determined that the width of the entire ZPR structure remains zero, indicating the presence of the ZPR effect. A range of geometric parameters have been established, inclusive of wall thickness t = 0.8 mm, 1.0 mm, and 1.2 mm. The arm length and inclination angle of the concave hexagonal element are expressed as l_1 = 16 mm and θ_1 = 60°, respectively. The arm length and inclination angle of the hexagonal element are expressed as l_2 = 8 mm and θ_2 = 120°, respectively. The length of l_3 in the ZPR element is determined and can be expressed as l_3 = 12 mm (Fig. 2).

2.2. Specimen manufacturing

Based on the melt deposition principle of 3D printer, SMP polylactic acid (PLA) filament with excellent shape memory performance and temperature-induced stiffness [82] was used as the printing material to print three cellular metamaterials. To ensure accurate and efficient printing, the printing speed of the printer was set at 30 mm/s, and with a melting temperature of 210 °C for the filament. The diameter of the printer nozzle is 0.4 mm, and the platform temperature of the printer was set at 50 °C. Fig. 3 shows samples of three Poisson's ratio cellular metamaterials. The envelope sizes of all samples are 96 mm × 90 mm × 30 mm.

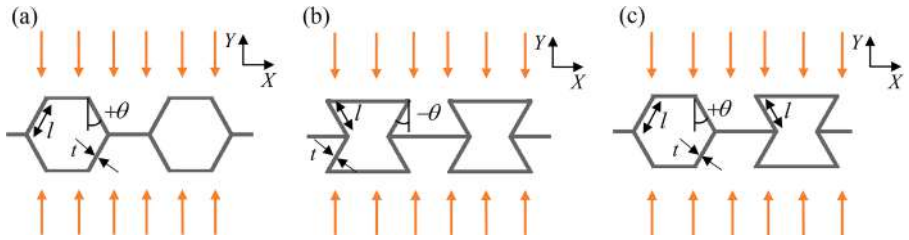

Fig. 1. Schematic diagram of honeycomb cell element under pressure (a) Schematic diagram of a regular hexagonal cell element under being compressed in the *Y* direction, (b) Schematic diagram of an NPR cell element being compressed in the *Y* direction, (c) Schematic diagram of a ZPR cell element consisting of alternating hexagonal and concave hexagonal cell elements being compressed in the *Y* direction.

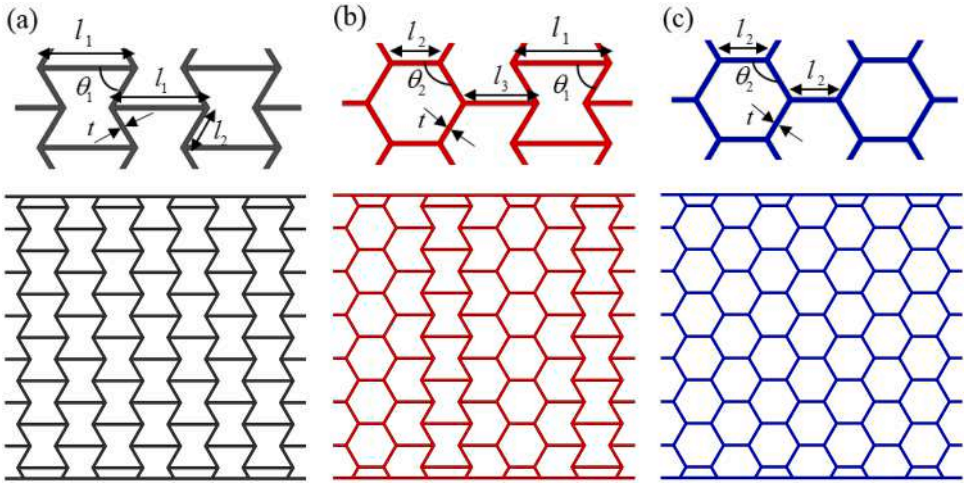

Fig. 2. Design and overall schematic of three cellular metamaterial cell elements (a) Dimensioning of NPR cell element, (b) Dimensioning of ZPR cell element, (c) Dimensioning of PPR cell element.

2.3. Compression mechanics experiment

The single-cell design of the metamaterial structure determines the mechanical properties and energy absorption capacity of the multi-cell metamaterial structure. To assess the mechanical properties and energy absorption capacity of three cellular metamaterials at variable temperatures, The SAAS Electronic Universal Testing Machine was used to perform the quasi-static compression test at variable temperatures. Four temperature conditions were selected namely 25 °C, 40 °C, 55 °C and 70 °C. The loading rate was set at 8 mm/min, and the loading lasted until the compacting stage of the specimen. To ensure the reproducibility of the experiments, the same type of samples was tested under identical conditions, three different times. A digital camera was employed to record the deformation patterns of the specimens during compression.

2.4. Tensile test of standard tensile specimens

The material properties of the metamaterial structures were first characterized. The acquired material properties were then applied to finite element simulations, to simulate the compressive deformation process of the three cellular metamaterials. PLA dog bone specimens were fabricated using fused deposition rapid prototyping 3D printing technology in accordance with ASTM standard D638. To precise printing, the printing speed of the tensile specimens was set to 30 mm/s at a melting temperature of 210 °C. The tensile specimens were printed in the direction of tensile force with a thickness of 1.7 mm. Experimental equipment and dimensions of the tensile specimens are illustrated in Fig. 4. Quasi-static isothermal tensile experiments were conducted at ambient temperatures of 25 °C, 40 °C, 55 °C and 70 °C for four types. The tensile test was conducted at a standard distance of 40 mm with a loading rate of 2 mm/min. Fig. 4(b) shows the true tensile stress-strain curves of the specimens. The elastic modulus of the material was obtained from the real stress-strain curve.

The glass transition temperature (*Tg*) is the temperature at which the material transitions from the glass state to the highly elastic state, which directly impacts the serviceability and processability of the material. The *Tg* of materials used is about 63 °C [35]. As shown in Fig. 4(b), when the temperature exceeds 55 °C and hits 70 °C, the tensile specimen's strength surpasses the strength of the material's strength at 55 °C. This is because the tensile specimens were fabricated using a 3D printer. This technique involves heating and melting the hot-melt material, which is then extruded through a nozzle. During the printing of the tensile specimens, the filaments of material extruded through the nozzle were bonded together layer by layer to form the printed structure. Microscopically, the interior of the tensile specimen consists of multiple printed filaments. At temperatures below the glass transition temperature, the material is in the glassy state and none of the molecular segments of the material can move. At temperatures slightly above the glass transition temperature, the molecular chain segments of the material begin to move marginally showing exceptional elastic properties. The molecular chains of a material become intertwined due to their movement, causing the printed filaments within the tensile specimens to bind closely together. Thus, the tensile strength of the tensile specimen at a temperature of 70 °C, is marginally greater than the tensile strength at 50 °C.

2.5. Simulation analysis

The compression and deformation mechanism of three cellular metamaterials was studied by ABAQUS/EXPLICIT 2020 simulation software. Three-dimensional finite element models of three cellular

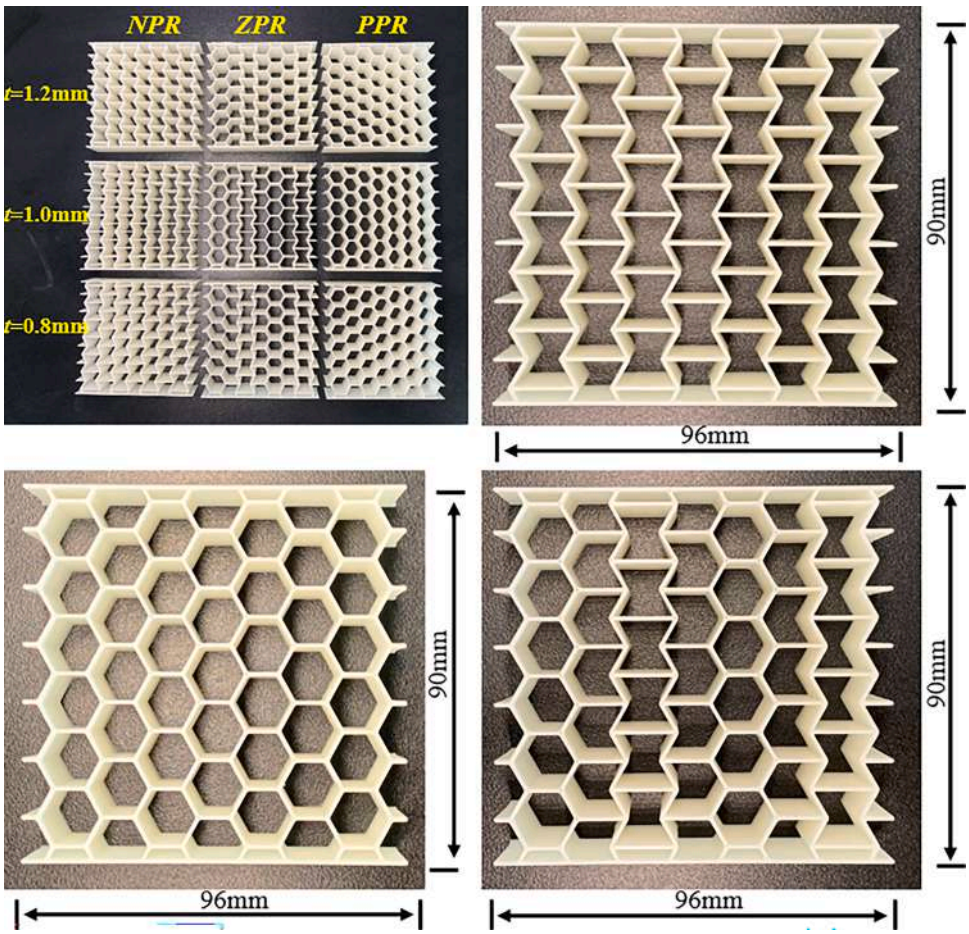

Fig. 3. Samples of three cellular metamaterials produced by 4D printing. Three cellular metamaterials were printed for each of the three wall thicknesses $t = 0.8$ mm, 1.0 mm, and 1.2 mm. The envelope sizes of all samples are 96 mm × 90 mm × 30 mm.

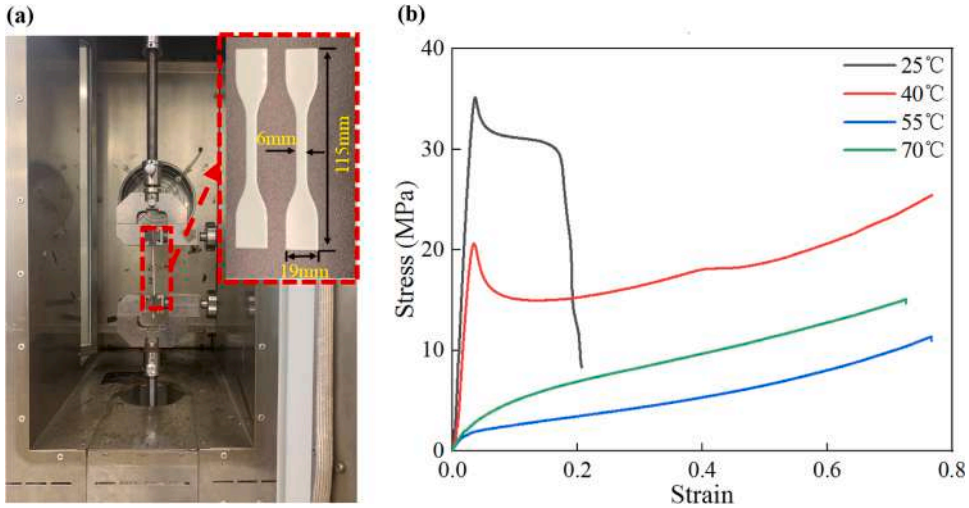

Fig. 4. (a) The experimental equipment and dimensions of the tensile specimens. The tensile specimens were printed in the tensile direction. (b) True stress-strain curves of tensile specimens at variable temperatures. The elastic modulus of the material is obtained by the real stress-strain curve.

metamaterials with three thicknesses were established according to the designed geometry. The hexahedral linear element (C3D8R) was used for grid division in the simulation model. To simulate the experimental state of compression of the structure in the simulation, rigid plates were placed on the upper and lower surfaces of the structure respectively. As shown in Fig. 6, the longitudinal direction in the face of the finite element structure is the *Y* direction, and the transverse direction in the face is the *X* direction. To guarantee the precision of the simulation, the rigid plate on the upper surface was moved downward at a uniform speed along the *Y* direction of the structural plane while the rigid plate on the lower surface was completely fixed. Simultaneously, the contact coefficient and friction characteristics of the model were determined,

and the convergence of the mesh was evaluated. In the finite element simulation, the friction coefficient for the tangential behavior in the pressure direction is 0.3 and the normal behavior is that of ``hard'' contact. Ultimately, each of the three cellular metamaterial models was divided into approximately 120,000 cells.

2.6. Behavioral representation of shape memory

Based on the special properties of SMP PLA material, all three cellular metamaterials obtained through 4D printing exhibit a shape memory effect. The *Tg* of materials used is about 63 °C [35]. To complete the shape memory cycle experiment systematically, the experiment was divided into three steps. In the first step, the specimen structure was heated at 70 °C (>*Tg*, rubbery state) and it was ensured that the structure was sufficiently heated. After that, the specimen structure was compressed by 30 mm with a loading rate of 8 mm/min, and the temperature was kept at 70 °C during this period. In the second step, the temperature of the test structure was lowered to ambient temperature (approximately 25 °C < *g*, the glassy state), and the mechanical load was removed after ensuring that the structure has cooled completely. In the third step, the temperature was increased again to 70 °C, which the temperature excites the shape memory effect of the specimen. Thus, the shape memory recovery process of the structure was obtained.

2.7. Vibration isolation capability of metamaterials

Metamaterials are widely used in the field of transportation, and their application is often accompanied by structural deformation [13, 83]. Thus, it is essential to evaluate the vibration isolation performance of the deformed metamaterials. Through the vibration measurement system, the vibration isolation characteristics of three cellular metamaterials were studied, showcased in Fig. 5. Attach the bottom of the cellular metamaterial to the retaining plate on the vibration exciter (MS-100 Shaker) and position a 200 g weight on the top of the cellular metamaterial. Employ epoxy adhesive to firmly fix the 200 g weight to the upper plate of the metamaterial. The signal generator delivered a sinusoidal swept signal ranging from 0–500 Hz for provision to the signal amplifier. The vibration load was generated by a vibration exciter. And the vibration was transmitted through the cellular metamaterial to the top of the structure and measured by an acceleration sensor (PCB PIEZOTRONICS LW254351). The input and output signals were collected and recorded by the signal acquisition instrument (DH5956).

3. Results and discussion

In this section, the compressive mechanical properties of three cellular metamaterials at ambient temperature were first analyzed. Subsequently, the compressive mechanical properties of three cellular metamaterials at variable temperatures were further analyzed, and the changes in compressive modulus and strength with temperature were also analyzed. Then, the absorption performance of the three metamaterials were calculated, compared and analyzed. To investigate the potential applications of 4D printed cellular metamaterials in deformable structures, shape recovery experiments were performed. Additionally, modal analysis was employed to determine the contribution of vibration deformation strain energy in three cellular metamaterials. Finally, the vibration isolation capacities of three cellular metamaterial structures at different deformation stages were tested and conclusions were obtained.

3.1. Compressive mechanical properties at ambient temperature

As shown in Fig. 6, the experimental data were processed to derive the equivalent force-strain response curve which accurately presents the force situation of the structure during compression. The equivalent compressive stress and equivalent compressive strain are defined as:

$$\sigma = F / A \tag{5}$$

$$\varepsilon = U / H \tag{6}$$

where F is the compression load, A is the compression cross-sectional area, $A = 96$ mm $\times$ 30 mm, U is the compression displacement, H is the total height of the specimen structure, and $H = 90$ mm.

To explore the compressive mechanical properties of three cellular metamaterials at ambient temperature, compression experiments were conducted on the specimens at ambient temperature. Fig. 6 shows the stress-strain curves of three cellular metamaterials at ambient temperature, including both experimental and simulated results. The carrying capacity of each of the metamaterials is approximately equivalent. Because of the uniform structure of the three cellular metamaterials, the stress fluctuations during compression are relatively smooth. Finite element simulation successfully predicted the compressive stress-strain reactions of all three cellular metamaterials. Fig. 6 substantiates that the simulation curve and the experimental compressive stress-strain curve exhibit good agreement.

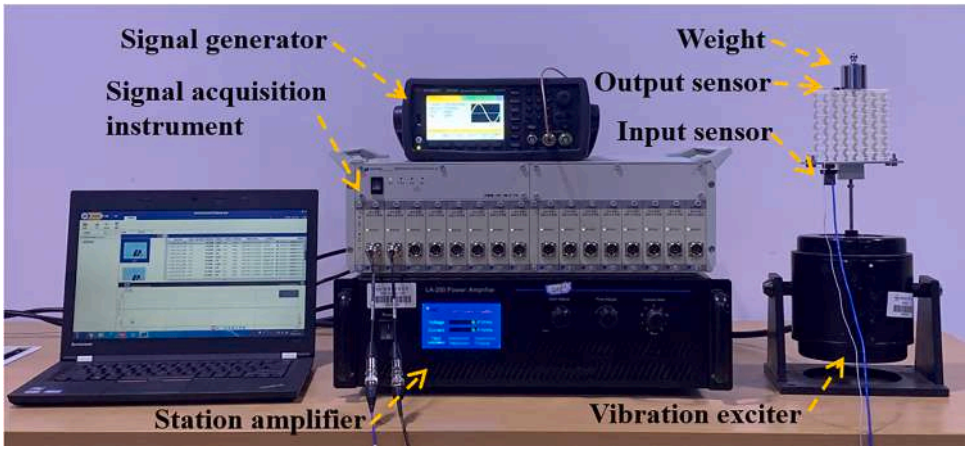

Fig. 5. Experimental equipment for vibration isolation characteristics test. The test principle is as follows: the signal generator produces a sinusoidal swept signal for input to the signal amplifier. The vibration load is generated by a vibration exciter, after which the vibration is transmitted through the cellular metamaterial to the top of the structure and measured by an acceleration sensor. The input and output signals are collected and recorded by the signal acquisition instrument.

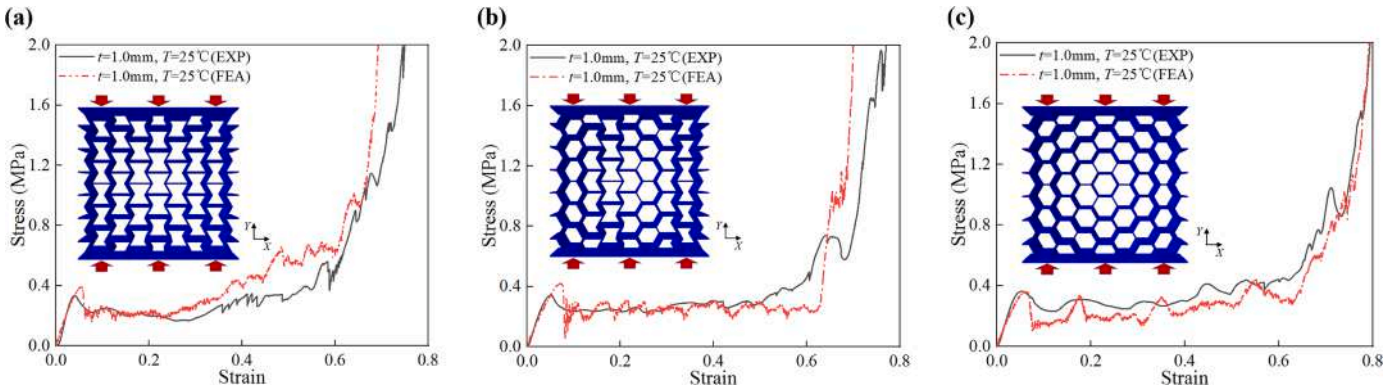

Fig. 6. Stress-strain curves of compression at ambient temperature and schematic structure of finite element simulation (a)NPR cellular metamaterial, (b)ZPR cellular metamaterial, (c)PPR cellular metamaterial.

3.2. Compressive mechanical properties at variable temperature

PLA is a thermoplastic material whose mechanical properties are greatly influenced by temperature. The *Tg* of materials used is about 63 °C [35]. To investigate the effect of temperature change on the mechanical properties of the three cellular metamaterials, compression experiments were conducted at 25 °C, 40 °C, 55 °C and 70 °C respectively. To explore the effect of structural cell element thickness on the mechanical properties of cellular metamaterials, variable temperature compression experiments and simulations were carried out on cellular metamaterials with structural cell element thicknesses of $t = 0.8$ mm, 1.0 mm, and 1.2 mm.

Figs. 7, 8, and 9 show the real stress-strain curves of three cellular metamaterials with different thicknesses at variable temperatures. The stress response of the cellular metamaterial decreases with the rise in temperature until the temperature reaches *Tg*. When the temperature exceeds the *Tg*, namely $Tg = 63$ °C, the fluctuations in the stress response are no longer evident. Finally, as temperature increases, the stiffness of the material decreases resulting in a smoother stress response curve for the cellular metamaterial. The SEA of all three cellular metamaterials increases as the wall thickness increases from 0.8 mm to 1.2 mm. Although the increase in wall thickness causes a rise in the mass of the metamaterial, it has a direct effect on the energy absorption capacity [35].

When comparing the stress-strain curves of the three cellular metamaterials, it can be observed that the stress-strain curves of the ZPR cellular metamaterial fluctuate more gently in the platform evolution stage. For the same mechanical load capacity, the flatter curve of the NPR allows it to be used without causing large stress perturbations during failure, which is a valuable feature. The dimensions of the metamaterial structures are perfectly accurate when modelled by finite element simulation. The nozzle diameter of the 3D printer used is 0.4 mm. The metamaterial structures printed by the 3D printer are subject to small size errors. Therefore, there is some deviation between the finite element simulation data and the experiment data. However, the trend of the curves is essentially the same.

The compressive modulus and compressive strength curves of the three cellular metamaterials with temperature are shown in Fig. 10. The compressive modulus is obtained by linearly fitting the initial value line segment of the stress-strain curve to the structure. The compression modulus of the three cellular metamaterials showed an S-shaped trend with temperature change. When the temperature is between 40 °C and 55 °C, the compression modulus of the structure decreases the fastest. When the temperature exceeds the *Tg* of the material, the compressive modulus of the structure becomes stable. When the structure temperature is close to *Tg*, the compression modulus of the three cellular metamaterials is approximately the same. The compressive strength of the structure in Fig. 10 is respectively the initial peak stress of the equivalent stress-strain curve. The three types of cellular metamaterials show a similar trend with the change in temperature.

Similar to the curves for the tensile specimens, the compressive modulus and strength of the cellular metamaterials show no tendency to decrease at temperatures slightly higher than the *Tg* of the material. When the cellular metamaterials were printed, the material filaments extruded through the nozzle were bonded together layer by layer to form the printed structure. Microscopically, the interior of the structure consists of multiple printed filaments. At temperatures below the glass transition temperature, the material is in the glassy state and none of the molecular segments of the material can move. At temperatures slightly above the glass transition temperature, the molecular chain segments of the material begin to move slightly and exhibit highly elastic properties. In this case, the moving molecular chain segments in the material make

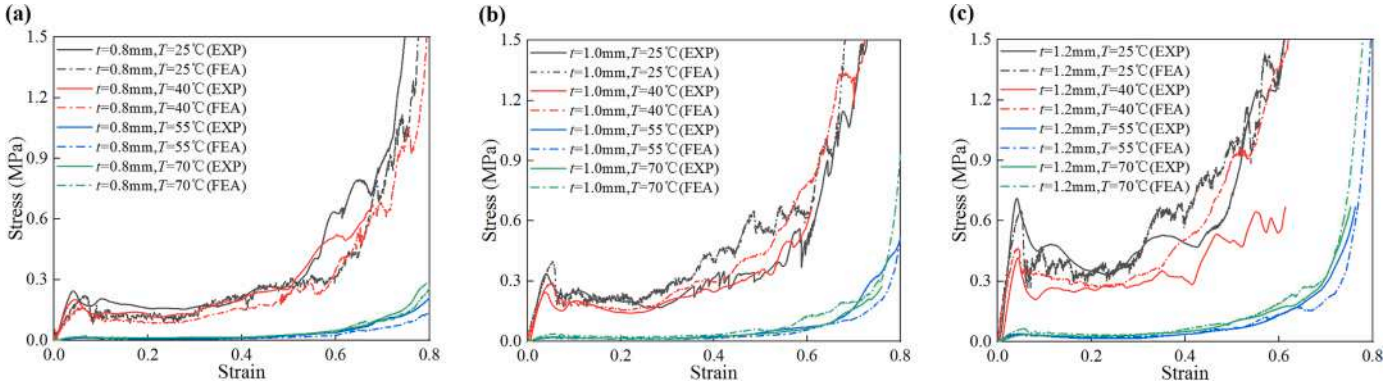

Fig. 7. Stress-strain curves of NPR cellular metamaterial of compression at ambient temperature (a) The wall thickness $t = 0.8$ mm, (b) The wall thickness $t = 1.0$ mm, (c) The wall thickness $t = 1.2$ mm.

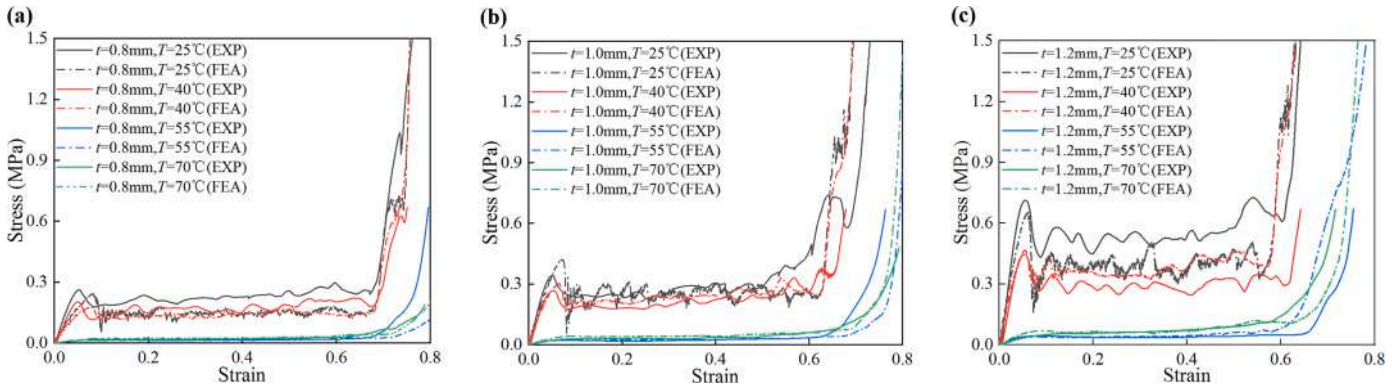

Fig. 8. Stress-strain curve of ZPR cellular metamaterial of compression at ambient temperature (a) The wall thickness $t = 0.8$ mm, (b) The wall thickness $t = 1.0$ mm, (c) The wall thickness $t = 1.2$ mm.

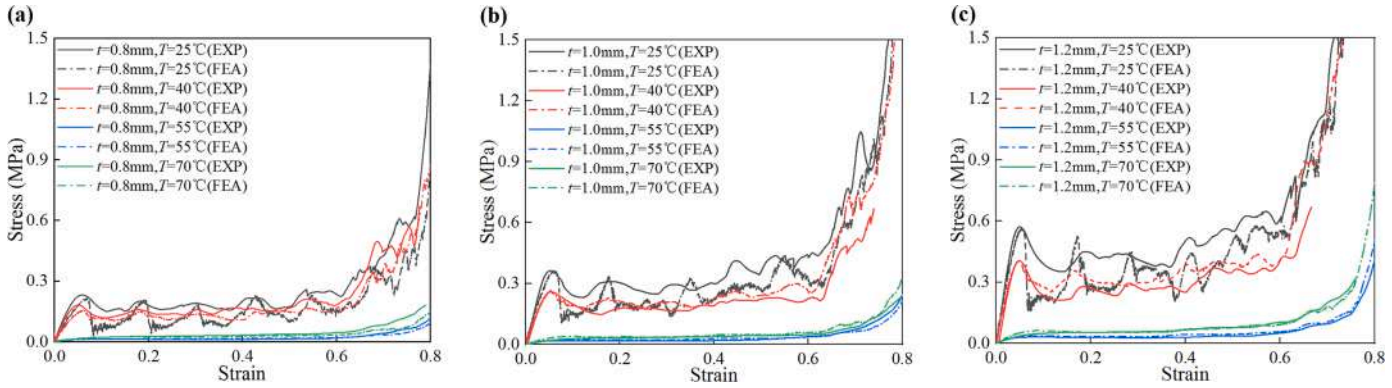

Fig. 9. Stress-strain curve of PPR cellular metamaterial of compression at ambient temperature (a) The wall thickness $t = 0.8$ mm, (b) The wall thickness $t = 1.0$ mm, (c) The wall thickness $t = 1.2$ mm.

the print filaments in the cellular metamaterials more tightly bound. As a result, the curves in Fig. 10 show such a trend.

3.3. Compression deformation characterization

The compression deformation characterization of the cellular metamaterials allows us to effectively observe the deformation pattern of the cellular metamaterials during the compression process. The deformation mode of the cellular metamaterial can effectively evaluate the mechanical properties and damage mechanism of the cellular metamaterial. Figs. 11, 12, and 13 show the deformation process of three cellular metamaterials with thickness $t = 1.0$ mm at variable temperatures. Four temperature conditions were selected namely 25 °C, 40 °C, 55 °C and 70 °C. The strain is 0,0.2083,0.4167 and 0.625 respectively.

Fig. 11 represents the experimental and simulated deformation process and comparison of the NPR cellular metamaterial. According to the Mises stress diagram, it is evident that the stiffness of the structure is higher at lower temperatures, and partial shear failure takes place during compression of the NPR cellular metamaterial. Due to the asymmetrical deformation of the metamaterial component element, the cell element folds and rotates, causing extensive buckling deformation of the entire metamaterial [78]. This leads to the NPR cellular metamaterial's instability. The buckling phenomenon occurs during the pre-compression stage, leaving the NPR cellular metamaterial not fully compressed. From Figs. 11 to 13, it can be seen that the NPR metamaterial structure is more prone to buckling during compression than the ZPR and PPR metamaterial structures. Therefore, the NPR metamaterial structure shown in Fig. 7 has an earlier stress recovery after the peak stress. As shown in Fig. 11, it can be observed that the asymmetric deformation of the metamaterial element occurs earlier as the temperature approaches *Tg* due to the premature failure of the defective nodes at the edges of the structure, resulting in a tendency for the deformation of the structure to tilt mainly to one side. The deformation model is also in agreement with the experimental results.

Fig. 12 represents the experimental and simulated deformation process and comparison of the ZPR cellular metamaterial. From the Mises stress diagram, it is clear that the ZPR cellular metamaterial generally showed uniform deformation during the compression process. The mutual compensation of positive and negative Poisson's ratio cells in the whole metamaterial structure makes the overall behavior zero. As the compressive strain increases, the lattice begins to collapse, eventually leading to structural densification. As the temperature increases, a depression on the right side of the structure shrinks during compression, causing the structure to tend to bend laterally during compression. The deformation model is also in agreement with the experimental results.

The experimental and simulated deformation process of the PPR cellular metamaterial is shown in Fig. 13. Different from the above two kinds of cellular metamaterials, the PPR cellular metamaterial will have significantly uneven deformation during the deformation process at low ambient temperature. During the compression process of the specimen, the deformation of the structure occurs mainly in the diagonal region of the structure. As the strain increases, the diagonal region of the structure begins to collapse layer by layer. Eventually, the lattice of the whole structure collapses. When the temperature is close to the *Tg*, the initial deformation of the structure is mainly in the middle region of the structure. As the strain increases, the whole structure collapses completely after the collapse of the central region of the structure. The deformation model is also in agreement with the experimental results.

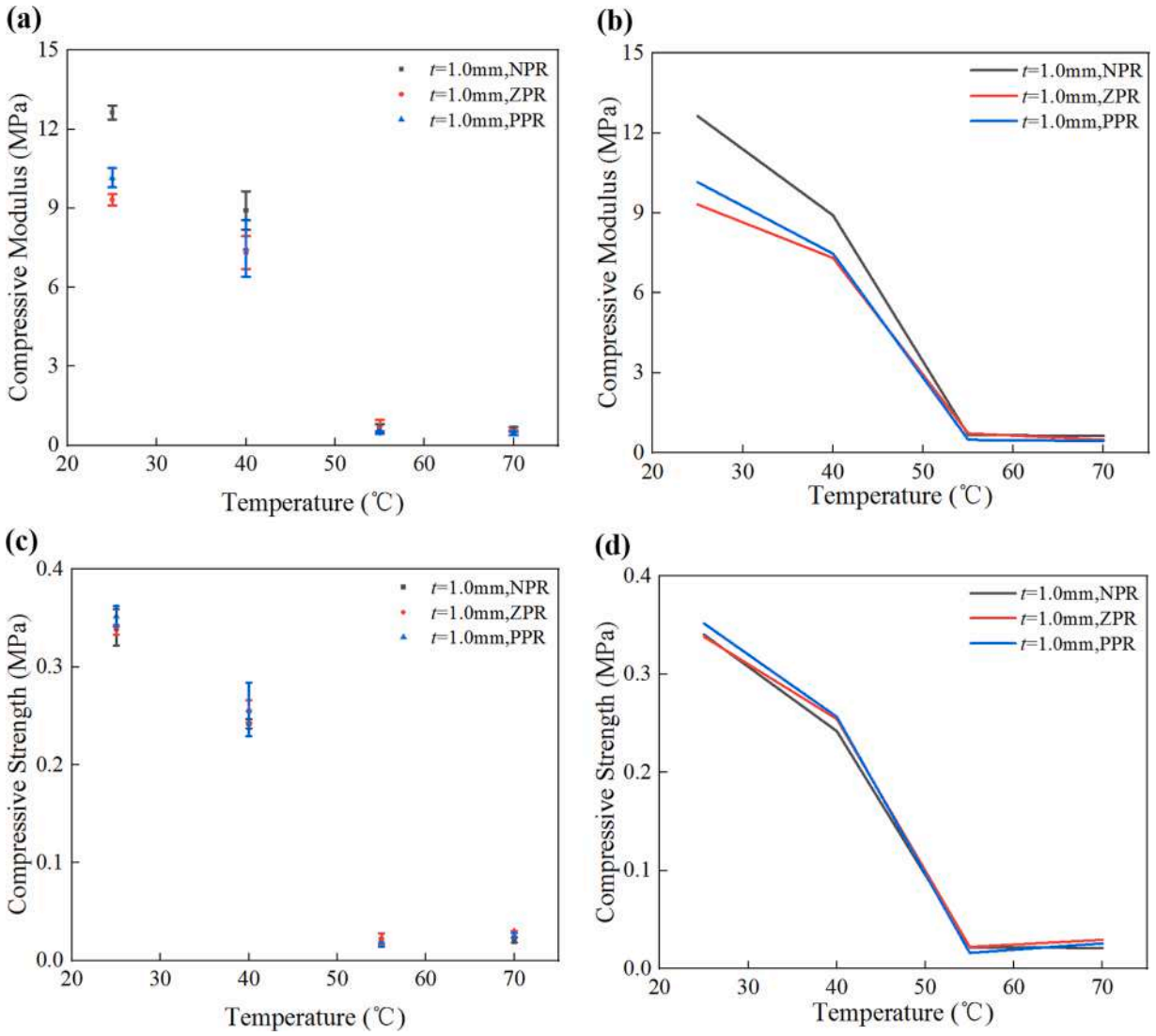

Fig. 10. (a) Experimental results of compression modulus variation with temperature, (b) Fitted plot of compression modulus, (c) Experimental results of compressive strength variation with temperature, (d) Fitted plot of compression strength.

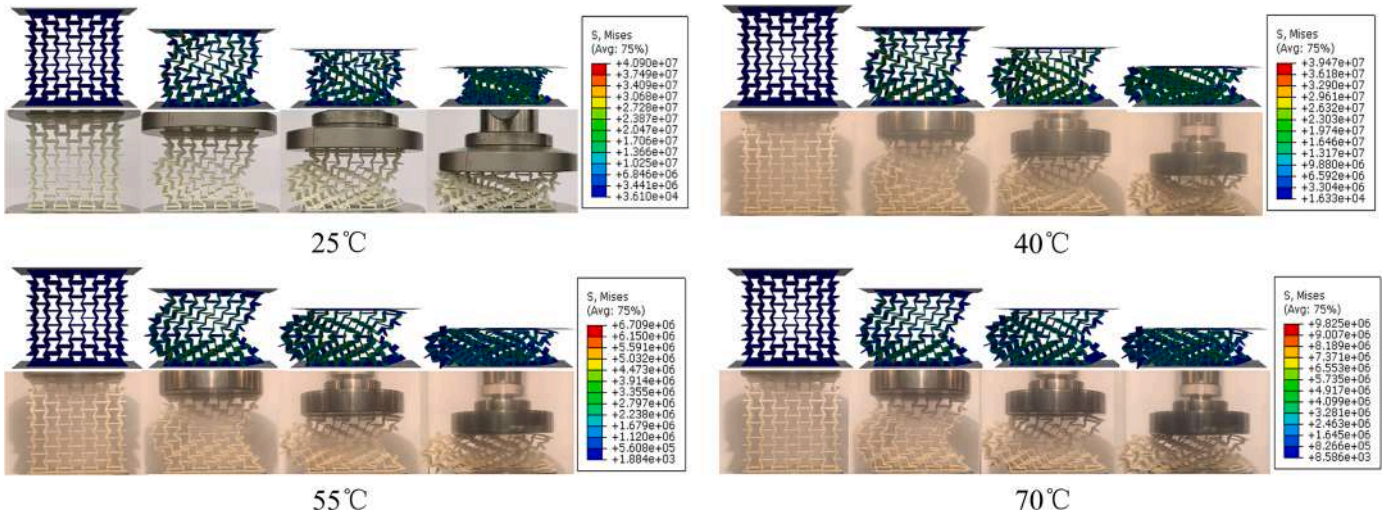

Fig. 11. Comparison of experimental and simulated deformation of NPR cellular metamaterial under compression at ambient temperature.

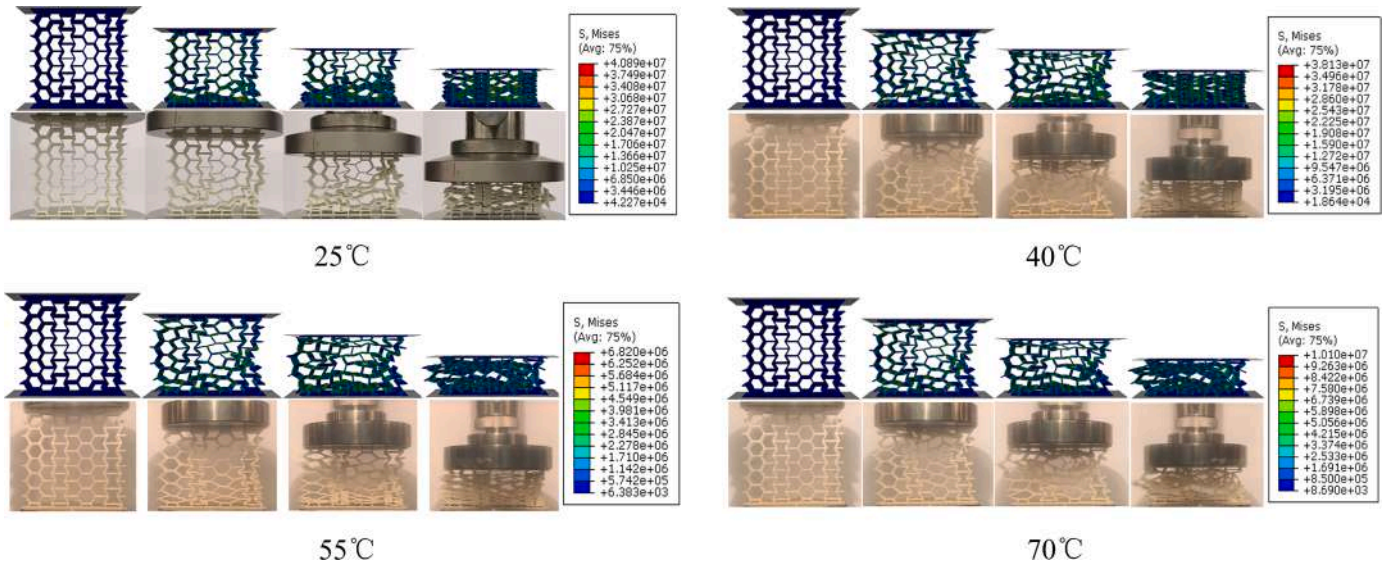

Fig. 12. Comparison of experimental and simulated deformation of ZPR cellular metamaterial under compression at ambient temperature.

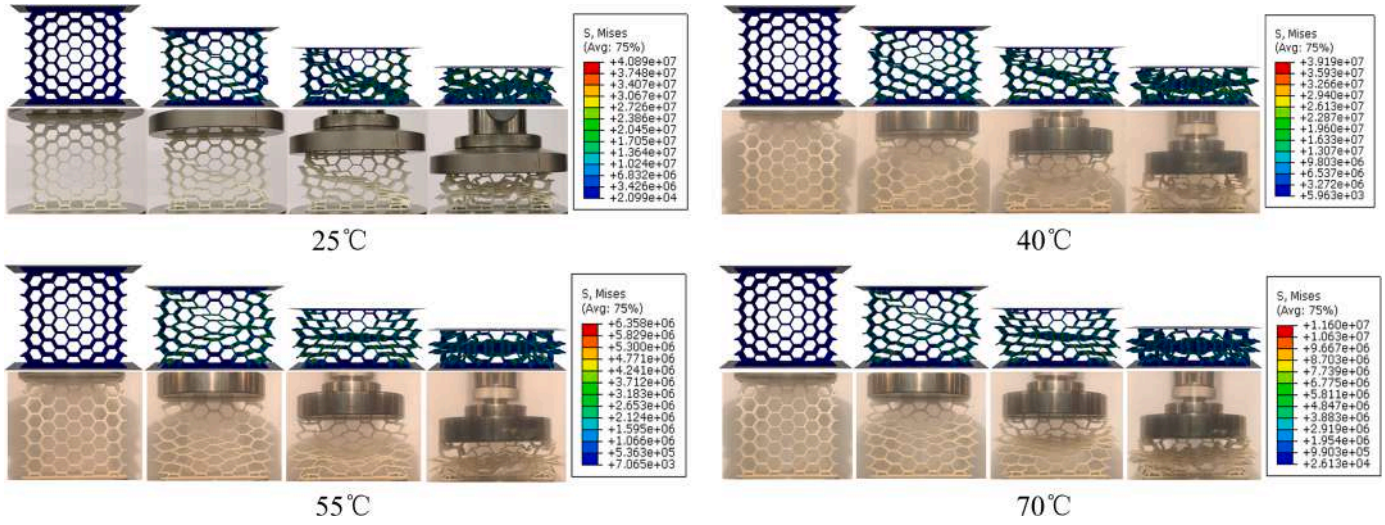

Fig. 13. Comparison of experimental and simulated deformation of PPR cellular metamaterial under compression at ambient temperature.

3.4. Absorption performance analysis

Specific energy absorption (*SEA*) is a common index to assess the energy absorption of a structure. The value of *SEA* is proportional to the energy absorption capacity of the structure. *SEA* generally indicates the energy absorbed per cell element mass and can be written as:

$$SEA = \frac{EA(\varepsilon)}{M} = \frac{E}{\rho} \tag{7}$$

where $EA(\varepsilon)$ is the energy absorbed when the axial deformation is ε. M is the weight of the energy-absorbing structure. E represents the energy absorption capacity per cell element volume structure. ρ represents the equivalent density of the cellular metamaterial. The area enclosed by stress curve and strain coordinates is used to represent the energy absorbed per cell element volume of the structure and can be written as:

$$E = \int_0^{\varepsilon_D} \sigma(\varepsilon) d\varepsilon \tag{8}$$

where ε_D represents the compacting strain of cellular metamaterial. The stress in a conventional multicellular material subjected to compression is an approximately constant straight line. The difference is that after the peak compressive stress, the stress in the Poisson's ratio mesh structure fluctuates above and below a constant value as the strain increases. As the strain continues to increase, the Poisson's ratio grid structure is further compressed. The stress on the stress-strain curve increases rapidly with increasing strain. At this point, the strain reaches the compacting strain of the grid structure.

The compacting strains of three kinds of cellular metamaterials with thickness $t = 1.0$ mm at variable temperatures were obtained by the fluctuation law of stress-strain curves. At 25 °C, 40 °C, 55 °C and 70 °C, the compacting strains (ε_D) of the three cellular metamaterials are about 0.6,0.6, 0.7 and 0.5, respectively. Fig. 14 shows the experimental data and finite element simulation of the *SEA* of three cellular metamaterials at variable temperatures. The *SEA* of all three cellular metamaterials decreases with increasing temperature. The *SEA* of three cellular metamaterials leveled off when the temperature exceeded the *Tg* of the material.

From Fig. 14, it can be concluded that the SEA of NPR and PPR cellular metamaterials is larger than ZPR cellular metamaterial at 25 °C and 40 °C. As can be seen from Fig. 10, this is due to the fact that the NPR and PPR cellular metamaterials have a higher stiffness than the ZPR

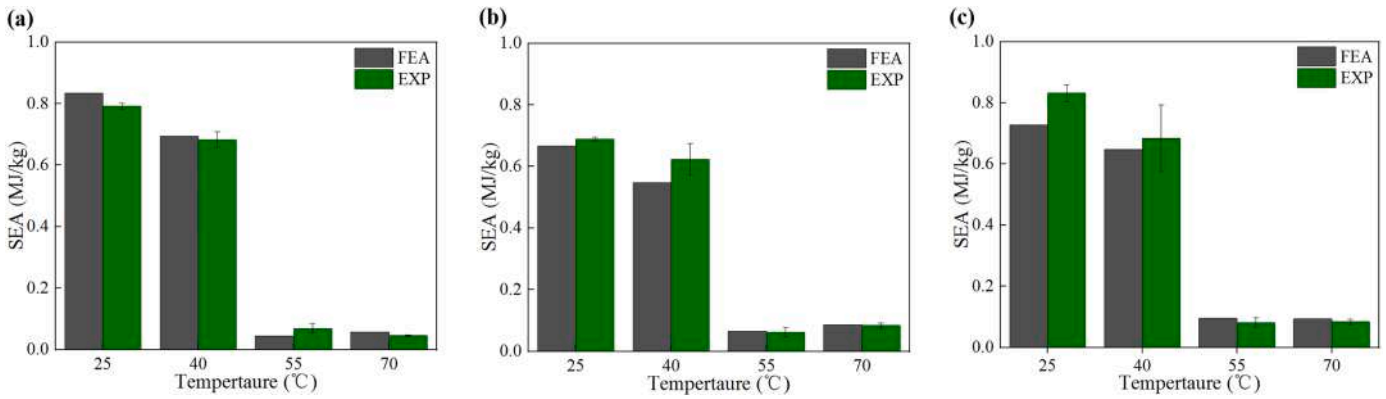

Fig. 14. Total energy absorption bar diagram of three cellular metamaterials during dense strain at ambient temperature (a) NPR cellular metamaterial, (b) ZPR cellular metamaterial, (c) PPR cellular metamaterial.

cellular metamaterial stiffness at this temperature. The SEA of NPR and ZPR cellular metamaterial is about the same when the temperature reaches 55 °C, and the SEA of PPR cellular metamaterial is the largest. When the temperature reaches 70 °C(>*Tg*, rubbery state), the SEA of ZPR and PPR cellular metamaterial is similar and the SEA of NPR cellular metamaterial is the minimum. The results show that the maximum energy absorption obtained by simulation is approximately the same as the experimental results.

Fig. 15 shows the relationship between *SEA* and equivalent strain of three cellular metamaterials at variable temperatures. In the primary stage, the structure is in the elastic region and absorbs less energy because its equivalent strain is too small. Then the cellular metamaterial enters the platform area. When the equivalent strain increases, the *SEA* of the structure increases. Then the cellular metamaterial enters the compacting area and the specific absorption energy increases rapidly with the increase of strain. As you can see in Fig. 15, the curves of the NPR cellular metamaterial at 50 °C and 70 °C are roughly coincident, and the *SEA* of the representative structures at 50 °C and 70 °C are roughly the same. ZPR cellular metamaterial 70 °C curve is slightly higher than 50 °C curve, which represents the structure 70 °C *SEA* slightly greater than the 50 °C *SEA*. The 70 °C curve of the PPR cellular metamaterial is higher than the 50 °C curve, which represents the *SEA* phase of the structure at 70 °C greater than 50 °C.

3.5. Mechanical behavior of shape memory

Due to the special properties of SMP PLA material, all three cellular metamaterials obtained by 4D printing have the shape memory effect. As shown in Fig. 16(a), three cellular metamaterials were heated at 70 °C (>*Tg*, rubbery state) and were compressed 30 mm at the same loading rate. In the cooling stage, the temperature was uniformly lowered from 70 °C to ambient temperature (approximately 25 °C < *Tg*, the glassy state), and the displacement at this stage was always maintained at 30 mm.

The mechanical load on the structure was removed at the end of the cooling phase. It is observed that the shapes of the structures do not change during the load removal process, indicating that the shape fixation rate of the 4D printed cellular metamaterials is close to 100 %. From the 480 s to the 1080s, the structure was in the shape recovery phase. As the temperature increased from 25 °C to 70 °C, the single cell of the cellular metamaterial started to return to its original shape due to the glass-rubber transition process of SMP. During this time, the shape memory effect of the cellular metamaterial was stimulated. It can be observed from Fig. 16(b) that the time-displacement curves of the three cellular metamaterials in the shape recovery process present an inverted S-shape.

The shape recovery rate can visually represent the journey of the structure back to its initial shape. The shape restoration ratio was defined as:

$$S = \frac{H_0 - H^*}{H_0} \times 100\% \tag{9}$$

where S denotes the shape restoration ratio of the structure, H_0 denotes the compression displacement of the structure after load unloading, and H^* denotes the residual displacement of the structure after shape restoration.

The curves in Fig. 16(b) show the shape recovery rates of the three cellular metamaterials. From Fig. 16(b), the final shape recovery rate of the NPR cellular metamaterial is the highest, but the shape recovery rate is slower at the beginning. The final shape recovery rate of the PPR

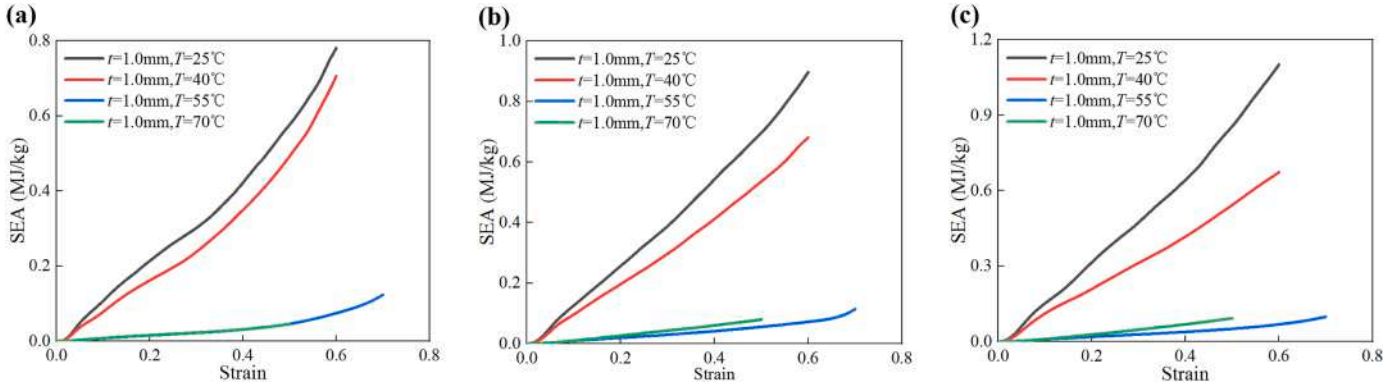

Fig. 15. Energy absorption curves of three cellular metamaterials during compacting strain at ambient temperature (a) NPR cellular metamaterial, (b) ZPR cellular metamaterial, (c) PPR cellular metamaterial.

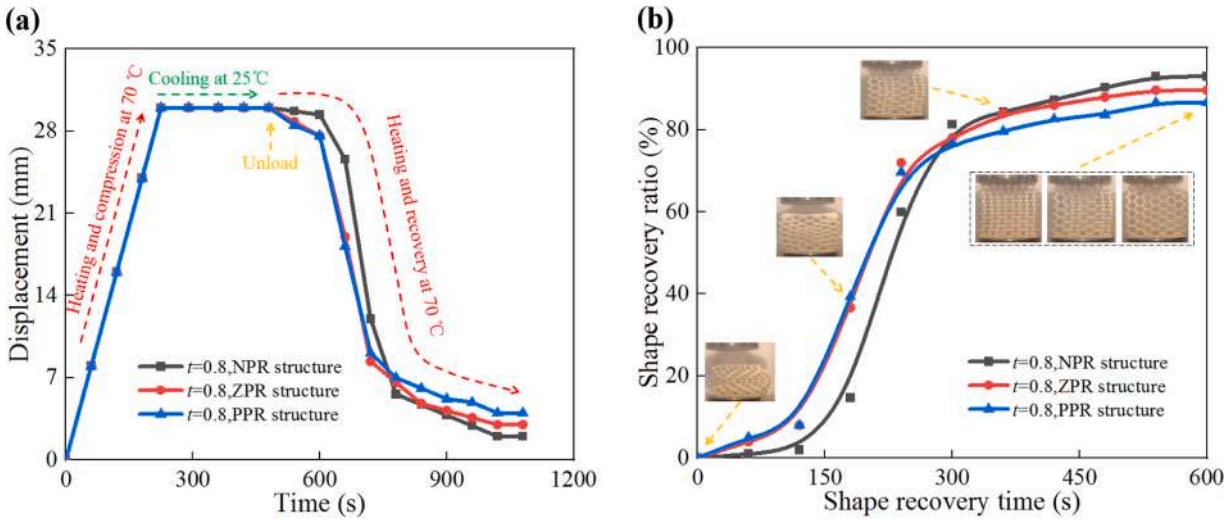

Fig. 16. Shape memory cycle experiment of 4D printed cellular metamaterials (a) Time-displacement curve. In the first 480 s, the three cellular metamaterials were heated at 70 °C and were compressed 30 mm at the same loading rate. In the cooling stage, the temperature is uniformly lowered from 70 °C to ambient temperature. After 480 s, the three cellular metamaterials were in the morphological recovery phase. (b) Recovery time-shape recovery rate curve. From the 480 s to the 1080 s in (a), the structure was at the stage of shape recovery. As the temperature rises from 25 °C to 70 °C, the single cell of the cellular metamaterial starts to return to its original shape due to the glass-rubber transition process of SMP. During this time, the shape memory effect of the cellular metamaterial is stimulated.

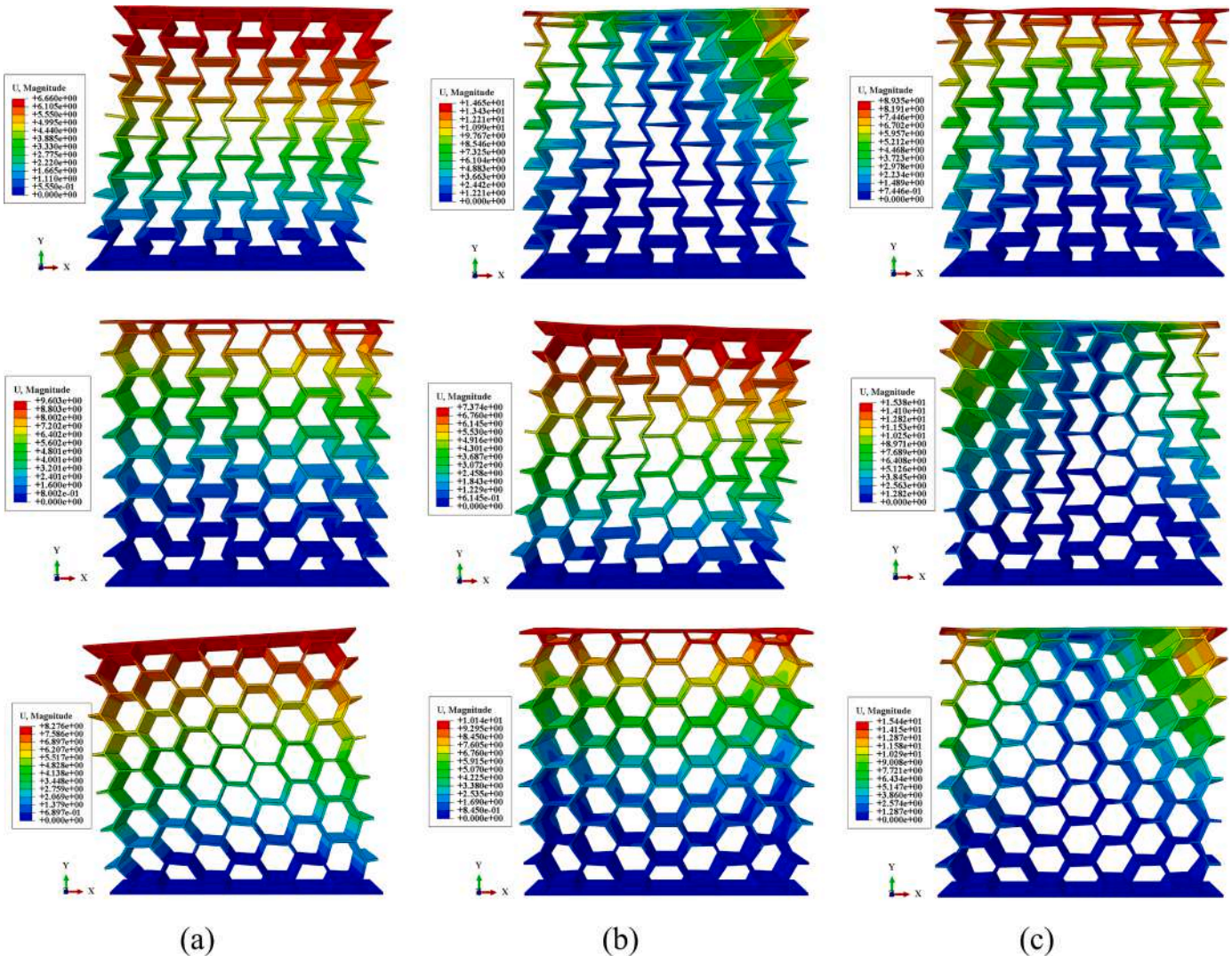

Fig. 17. The mode shapes of the NPR, ZPR, and PPR cellular metamaterials in the first three orders (a) 1st-order mode, (b) 2nd-order mode, and (c) 3rd-order mode.

cellular metamaterial is lower, but the shape recovery rate is faster at the beginning. The final shape recovery rate of the ZPR cellular metamaterial is between NPR and PPR, and the initial shape recovery rate is about the same as that of the PPR cellular metamaterial. The NPR cellular metamaterial has the highest shape recovery ratio compared to the PPR and ZPR cellular metamaterials. As shown in Fig. 11, this is due to the fact that the NPR cellular metamaterial is prone to structural buckling during compression. The cellular elements of the structure are less damaged during compression, so the NPR cellular metamaterial can more easily return to its initial shape during shape recovery. The shape recovery ratio of the NPR cellular metamaterial is 93.00 %. The shape recovery ratio of ZPR cellular metamaterial is 89.67 %. And the shape recovery ratio of PPR cellular metamaterial is 86.67 %.

3.6. Contribution rate of strain energy to vibration deformation

To investigate the contribution rate of vibrational deformation strain energy of three cellular metamaterials, modal analysis was performed for three cellular metamaterials with wall thickness $t = 0.8$ mm. For the modal analysis, the bottom of the three models was completely fixed and the top was free. As shown in Fig. 17, the longitudinal direction in the face of the finite element structure is the *Y* direction, and the transverse direction in the face is the *X* direction. The first three orders of vibration shapes of the structure were calculated by selecting the Lanczos method through the modal analysis step in the ABAQUS simulation software. At the same time, the values of the stress and strain components for the corresponding mode shapes were obtained from the results of the calculations. The first three modes of the three cellular metamaterials are shown in Fig. 17. The first three orders of intrinsic frequencies of the NPR cellular metamaterial are 76.999 Hz,124.92 Hz and 133.30 Hz. The first three orders of intrinsic frequency for ZPR cellular metamaterial are 109.17 Hz,109.45 Hz and 153.08 Hz. And the first three orders of intrinsic frequency for PPR cellular metamaterial are 109.17 Hz,109.45 Hz and 153.08 Hz.

The main loss source of the structure was analyzed by simulating the damping characteristics of each mode. From the ABAQUS modal analysis results, the volume of each cell and the stress and strain components of each cell in all directions can be extracted. The strain energy components and the total strain energy of each cell element of the structural simulation model were calculated using data post-processing program. For ease of presentation, the *X, Y* and *Z* directions are denoted by 1, 2 and 3 respectively. SE11, SE22, SE33, SE12, SE13, and SE23 are used to represent the strain energy components in directions *XX, YY, ZZ, XY, XZ*, and *YZ*, respectively. As the strain energy component in the *YZ* direction is small in each mode, it is ignored. The strain energy components in each direction of the structure in each modal deformation were obtained by calculation. Then the main loss sources of the structure were analyzed according to the strain energy component that plays a major role.

As can be seen from Fig. 17, the *X* and *Y* directions represent the transverse and longitudinal directions of the cellular metamaterial, respectively. Fig. 18 shows that the strain energy in the first mode of the NPR cellular metamaterial mainly comes from SE11. The energy dissipation of the structure by deformation mainly comes from the deformation energy in the *X* direction. In the first mode of the ZPR cellular metamaterial, the strain energy mainly comes from SE22 and SE12. The energy dissipated by deformation is mainly derived from the deformation energy in the *Y* direction and the shear direction in the *X-Y* plane. In the first mode of the PPR cellular metamaterial, the strain energy mainly comes from SE11 and SE12. The energy dissipated by deformation is mainly derived from the deformation energy in the *X* direction and the shear direction in the *X-Y* plane. In comparison, the ZPR cellular metamaterial has more strain energy and better damping in the *Y* direction, which can be better applied to vibration isolation structures.

3.7. Structural vibration isolation and damping experiment

The low frequency negative vibrational energy level difference (VLD) is an important property of cellular metamaterials, which is rarely found in conventional vibration isolation elements. Conventional vibration isolation elements (such as springs) are difficult to use in reducing low frequency vibrations in structures. To investigate the vibration isolation capacity of three cellular metamaterial structures in different deformation stages, the vibration isolation characteristics of three cellular metamaterials were tested using the equipment shown in Fig. 5. During the experiment, the acceleration signals at the bottom and top of the structure were received by the sensors (PCB PIEZOTRONICS LW254351). Fig. 19(a) represents the curves of input and output signal amplitude versus time. The input and output time domain signals were Fourier transformed to obtain their frequency domain signals, and the peaks of the frequency-domain signals correspond to the natural frequencies of the structure. And Fig. 19(b) represents the curves of the input signal and output signal amplitude versus frequency. The vibration isolation capacity of the structure is described by calculating the VLD.

$$VLD = 20\lg\left(a_{output} \,/\, a_{input}\right) \tag{10}$$

Since the printing materials used for the three cellular metamaterials have excellent shape recovery properties, the cellular metamaterials can be restored from a certain compressed state to the initial height according to the actual requirements. When the cellular metamaterial

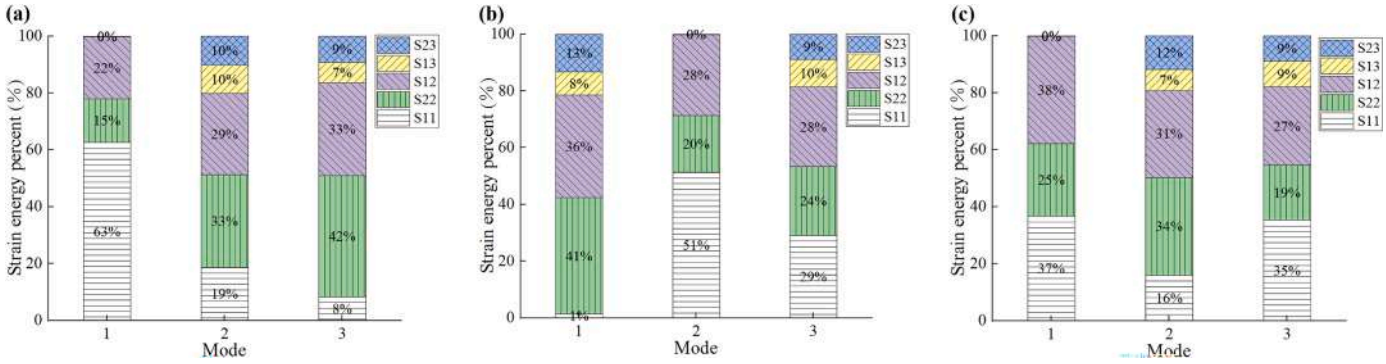

Fig. 18. Strain energy contributions of three cellular metamaterials in the first three orders of modes, (a) NPR cellular metamaterial. The strain energy in the first mode of the NPR cellular metamaterial mainly comes from SE11. The energy dissipation of the structure through deformation mainly comes from the deformation energy in the *X* direction. (b) ZPR cellular metamaterial. In the first mode of ZPR cellular metamaterial, the strain energy mainly comes from SE22 and SE12. The energy dissipated by deformation is mainly derived from the deformation energy in the *Y* direction and the shear direction in the *X-Y* plane. (c) PPR cellular metamaterial. In the first mode of PPR cellular metamaterial, the strain energy mainly comes from SE11 and SE12. The energy dissipated by deformation is mainly derived from the deformation energy in the *X* direction and the shear direction in the *X-Y* plane.

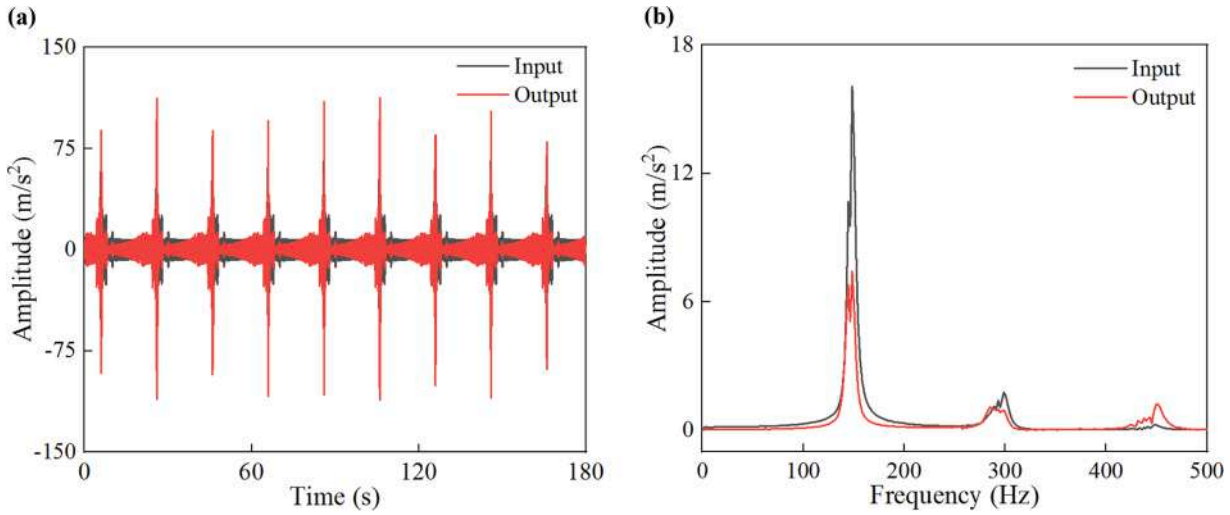

Fig. 19. (a) Input and output acceleration amplitude curves versus time, (b) Input and output acceleration amplitude curves versus frequency. The input and output time-domain signals are Fourier transformed to obtain their frequency-domain signals, and the peaks of the frequency-domain signals correspond to the natural frequencies of the structure.

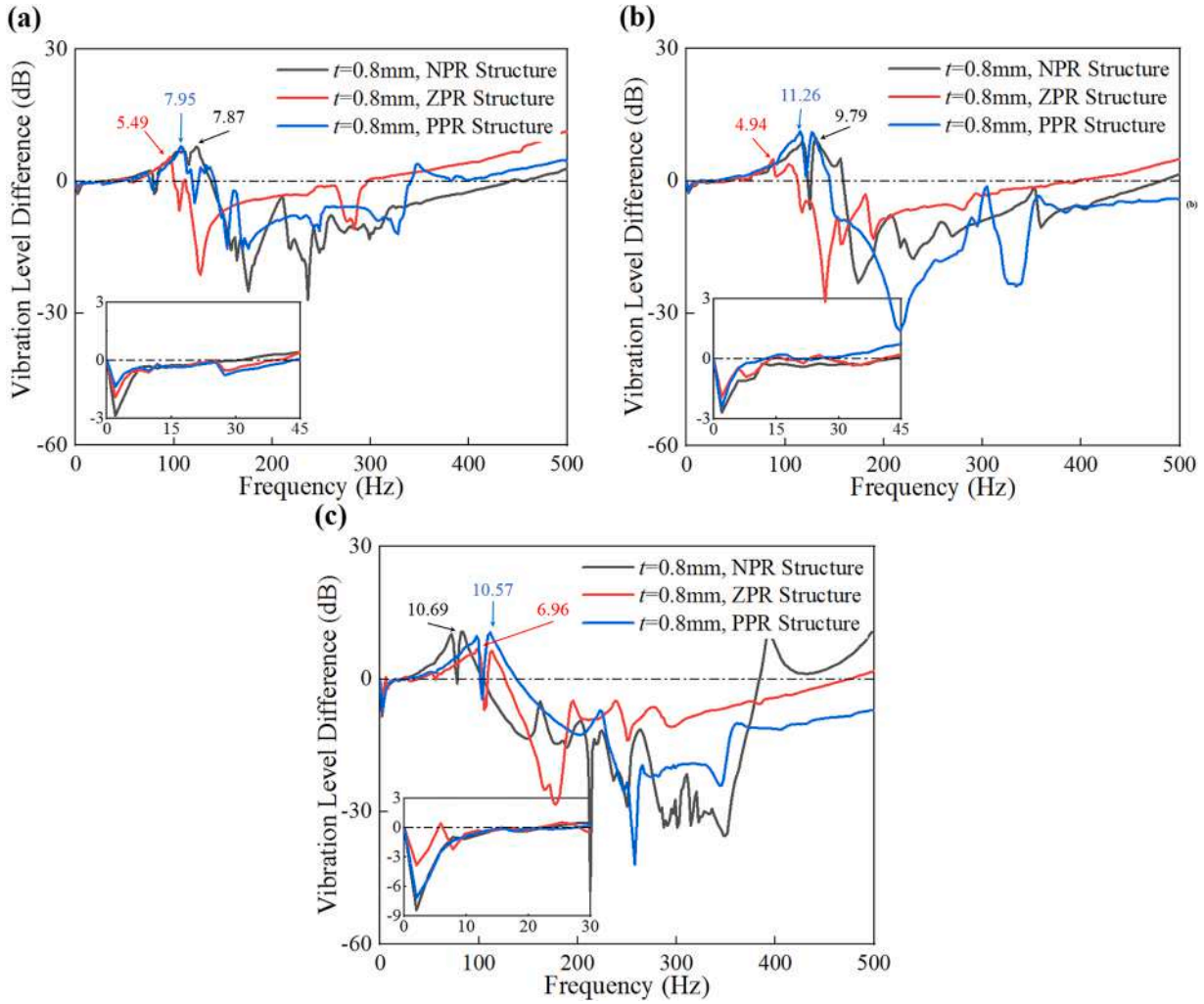

Fig. 20. VLD curves of three cellular metamaterials at different heights, (a) The height of the structures is 90 mm, (b) The height of the structures is 80 mm, (c) The height of the structures is 70 mm. The VLD of the ZPR cellular metamaterial is negative at 0–37 Hz and 101 Hz–295 Hz, and the maximum VLD is 5.49 dB. The VLD values of the PPR cellular metamaterial are negative at 0–41 Hz and 142 Hz–339 Hz, and the maximum VLD value is 7.95 dB. When the VLD is negative, the structure shows good vibration isolation capability.

returns from a certain compression state to its initial height, its vibration isolation capacity also changes. In order to investigate the vibration isolation capacity of three cellular metamaterials under different compression states, vibration isolation test experiments were conducted on them after they were compressed to a certain height, and the corresponding VLDs were obtained by calculation.

When the VLD value is less than zero, it means that the vibration acceleration signal is reduced by the cellular metamaterial. The magnitude of the negative value of VLD indicates the vibration isolation capability of the cellular metamaterial. Fig. 20 shows the frequency variation curve of VLD values of three cellular metamaterials with a thickness of 0.8 mm. Tables 1, 2 and 3 are the numerical statistics of the curves in Fig. 20(a)–(c).

It can be seen from Fig. 20(a) that when the structures are in their initial shapes, the VLD of the NPR cellular metamaterial is negative at 0–30 Hz and 138 Hz–440 Hz, and the highest VDL is 7.87 dB. The VLD of the ZPR cellular metamaterial is negative at 0–37 Hz and 101 Hz–295 Hz, and the maximum VLD is 5.49 dB. The VLD values of the PPR cellular metamaterial are negative at 0–41 Hz and 142 Hz–339 Hz, and the maximum VLD value is 7.95 dB. When the VLD is negative, the structure shows good vibration isolation capability.

After the three cellular metamaterials were compressed to 80 mm, the VLD of the three structure shapes was calculated, as shown in Fig. 20 (b). Compared with the initial VLD of the structure, the negative interval of the NPR cellular metamaterial at low frequency increases to 0–41 Hz, the negative interval of the ZPR cellular metamaterial at low frequency is 0–22 Hz and 27 Hz–39 Hz, and the negative area of the PPR cellular metamaterial at low frequency decreases to 0–12 Hz and 19 Hz–23 Hz. Then, the three cellular metamaterials were compressed to 70 mm, and the VLD of the three structural shapes was calculated, as shown in Fig. 20(c). Compared with the initial VLD of the structure, the negative region of the NPR cellular metamaterial at low frequency is reduced to 0–21 Hz, the negative region of the ZPR cellular metamaterial at low frequency is 0–22 Hz and 29 Hz–37 Hz, and the negative region of the PPR cellular metamaterial at low frequency decreases to 0–27 Hz.

From the data in the table, it can be obtained that the maximum VLD values of ZPR cellular metamaterial at all three deformation heights are lower than those of the other two cellular metamaterials in the low frequency range. After compression, the ZPR cellular metamaterial also has maximum vibration isolation zone at low frequencies. The results demonstrate that the cellular metamaterials with ZPR possess superior vibration isolation capability compared to NPR or PPR cellular metamaterials, which have great potential for applications in manufacturing and industry. Incorporating adjustable metamaterials into car seats to diminish passenger vibration represents a promising utilization [84]. At the same time, the use of metamaterial deformation to regulate the vibration isolation performance of the structure at low frequencies is of great research value.

4. Conclusion

In this study, to further explore the properties of cellular metamaterials, three types of cellular metamaterials with negative/zero/positive Poisson's ratio and vibration isolation effects were designed and fabricated based on 4D printing of shape memory polymers. First, the compressive properties and energy absorption capacity of the three cellular metamaterials at variable temperatures were evaluated by finite element simulations and compression experiments. The deformation modes and damage mechanisms of three cellular metamaterials at variable temperatures were revealed. To explore the application possibilities of 4D printed cellular metamaterials in deformable structures, shape recovery experiments were performed. Finally, the vibration isolation capabilities of three cellular metamaterials at different deformation stages were tested and conclusions were obtained. The following conclusions have been drawn.

The three cellular metamaterials demonstrate dissimilar energy absorption capabilities and shape deformations at various temperatures. NPR and PPR cellular metamaterials exhibit greater absorption capacity at lower temperatures, whereas ZPR and PPR cellular metamaterials demonstrate superior energy absorption at temperatures close to *Tg*. The three metamaterials undergo varied deformation when compressed at varying temperatures. In compression, the NPR cellular metamaterial exhibits substantial structural buckling, whereas the PPR cellular metamaterial does not display significant buckling.

To investigate the potential applications of 4D printed cellular metamaterials in deformable structures, shape recovery experiments were conducted. The findings indicated that all three types of cellular metamaterials possessed a notable shape recovery rate (in excess of 86.67 %).

The maximum VLD values of ZPR cellular metamaterial at all three deformation heights are lower than those of the other two cellular metamaterials in the low frequency range. Additionally, the ZPR cellular metamaterial exhibits a maximum vibration isolation zone at low frequencies after compression. These findings indicate that ZPR cellular metamaterials possess superior vibration isolation capabilities compared to NPR or PPR cellular metamaterials.

Based on research into the mechanical properties, energy properties, shape memory, and vibration isolation effects of cellular metamaterials, this provides a valuable reference for the development of cellular metamaterials that can meet specific functional requirements. Consequently, this research constitutes a dependable guide for applying cellular metamaterials in areas such as traditional architecture, innovative wings, automotive engineering, nanotechnology, and biomedicine.

Table 1
Numerical statistics of VLD curves of cellular metamaterials with a height of 90 mm.

$H = 90$ mm	The highest VDL/dB	Low frequency range of negative VLD/Hz	High frequency range of negative VLD/Hz
NPR	7.87	0–30	138–440
ZPR	5.49	0–37	101–295
PPR	7.95	0–41	142–339

Table 2
Numerical statistics of VLD curves of cellular metamaterials with a height of 80 mm.

$H = 80$ mm	The highest VDL/dB	Low frequency range of negative VLD/Hz	High frequency range of negative VLD/Hz
NPR	9.79	0–41	160–480
ZPR	4.94	0–22, 27–39	113–394
PPR	11.26	0–12, 19–23	146–500

Table 3
Numerical statistics of VLD curves of cellular metamaterials with a height of 70 mm.

$H = 70$ mm	The highest VDL/dB	Low frequency range of negative VLD/Hz	High frequency range of negative VLD/Hz
NPR	10.69	0–21	105–382
ZPR	6.96	0–22, 29~37	126–472
PPR	10.57	0–27	138–500

CRediT authorship contribution statement

Peilei Xu: Conceptualization, Investigation, Visualization, Formal analysis, Writing – original draft, Writing – review & editing. **Xin Lan:** Methodology, Data curation, Validation, Writing – review & editing. **Chengjun Zeng:** Visualization, Data curation, Writing – review & editing. **Xudong Zhang:** Visualization, Data curation, Writing – review

& editing. **Hanxing Zhao:** Visualization, Data curation, Writing – review & editing. **Jinsong Leng:** Investigation, Writing – review & editing, Supervision. **Yanju Liu:** Conceptualization, Investigation, Writing – review & editing.

Declaration of Competing Interest

We declare that we do not have any commercial or associative interest that represents a conflict of interest in connection with the work submitted.

Data availability

Data will be made available on request.

Acknowledgments

This work is supported by the National Natural Science Foundation of China (Grant no. 12072094).

References

[1] Evans AG, Hutchinson JW, Fleck NA, Ashby MF, Wadley HNG. The topological design of multifunctional cellular metals. Prog Mater Sci 2001;46:309–27.
[2] Deshmukh S, Kumar S, Wagh A, Krishnan S, Ramamoorthy S. Selection of periodic cellular structures for multifunctional applications directly based on their unit cell geometry. Int J Mech Sci 2022;220:107133.
[3] Lin WH, She CM, Zhang CY, Branicio PS, Sha ZD. Tuning the mechanical properties of cellular metallic glasses. Int J Plasticity 2022;156:103373.
[4] Hohe J, Becker W. Effective elastic properties of triangular grid structures. Compo Struct 1999;45:131–45.
[5] Zhang Q, Wu WW, Liu JL. Local strengthening design and compressive behavior study of the triangular honeycomb structure. Metals 2022;12:1779.
[6] Song H, Zhang CY, Wang PY, Min BZ, Wang ZQ. In-plane impact resistance of a diamond-shaped hierarchical honeycomb. Adv Mater Sci Eng 2022;2022:6301537.
[7] Queheillalt DT, Carbajal G, Peterson GP, Wadley HNG. A multifunctional heat pipe sandwich panel structure. Int J Heat Mass Transf 2008;51:312–26.
[8] Yu C, Wang QF, Xia ZH, Wang YJ, Mei C, Liu YH. Multiscale topology optimization for graded cellular structures based on level set surface cutting. Struct Multidiscip Optim 2022;65:32.
[9] Shanta FA, Bari MAA. Experimental and numerical investigation on honeycomb, modified honeycomb, and spiral shapes of cellular structures. Struct Eng Mech 2022;84:665–73.
[10] Liu H, Zhang ET, Wang GJ, Ng BF. In-plane crushing behavior and energy absorption of a novel graded honeycomb from hierarchical architecture. Int J Mech Sci 2022;221:107202.
[11] Davalos JF, Qiao PZ, Xu XF, Robinson J, Barth KE. Modeling and characterization of fiber-reinforced plastic honeycomb sandwich panels for highway bridge applications. Compos Struct 2001;52:441–52.
[12] Lei ZW, Sun XT, Zhu SF, Dong K, Liu XQ, Wang LL, et al. Nature inspired MXene-decorated 3D honeycomb-fabric architectures toward efficient water desalination and salt harvesting. Nano-Micro Lett 2022;14:10.
[13] Heo H, Ju J, Kim DM. Compliant cellular structures: application to a passive morphing airfoil. Compos Struct 2013;106:560–9.
[14] Gong XB, Ren CW, Sun J, Zhang PR, Du L, Xie F. 3D zero Poisson's ratio honeycomb structure for morphing wing applications. Biomimetics 2022;7:198.
[15] Solak A, Temiztas BA, Bolat B. Numerical investigation of the mechanical behavior of the vertical stabilizer leading edge with wavy honeycomb sandwich structure under bird strike. J Sandw Struct Mater 2023;25:387–400.
[16] Masuda H, Fukuda K. Ordered metal nanohole arrays made by a two-step replication of honeycomb structures of anodic alumina. Science 1995;268:1466–8.
[17] Gadkaree KP. Carbon honeycomb structures for adsorption applications. Carbon 1998;36:981–9.
[18] Gao W, Zhang WH, Yu HP, Xing WE, Yang XL, Zhang YG, et al. 3D CNT/MXene microspheres for combined photothermal/photodynamic/chemo for cancer treatment. Front Bioeng Biotechnol 2022;10:996177.
[19] Yu J, Feng YF, Sun D, Ren WF, Shao CY, Sun RC. Highly conductive and mechanically robust cellulose nanocomposite hydrogels with antifreezing and antidehydration performances for flexible humidity sensors. ACS Appl Mater Interfaces 2022;14:10886–97.
[20] Liu JY, Liu HT, An MR. Crushing behaviors of novel Diabolo shaped honeycombs with enhanced energy absorption performance. Int J Mech Sci 2022;229:107492.
[21] Xu MC, Xu ZR, Zhang Z, Lei HS, Bai YC, Fang DN. Mechanical properties and energy absorption capability of AuxHex structure under in-plane compression: theoretical and experimental studies. Int J Mech Sci 2019;159:43–57.
[22] Zhang QQ, Dong JQ, Zhao YT, Zheng YY. Three-dimensional meta-architecture with programmable mechanical properties. Int J Smart Nano Mater 2022;13:152–65.
[23] Dong JH, Ye GY, Wang YJ, Jin FNA, Fan HL. Design, manufacture and crushing behaviors of buckling-inspired auxetic meta-lattice structures. Int J Smart Nano Mater 2021;12:491–510.
[24] Niu XQ, Xu FX, Zou Z, Fang TY, Zhang S, Xie QM. In-plane dynamic crashing behavior and energy absorption of novel bionic honeycomb structures. Compos Struct 2022;299:116064.
[25] Berger JB, Wadley HNG, McMeeking RM. Mechanical metamaterials at the theoretical limit of isotropic elastic stiffness. Nature 2017;543:533.
[26] Geramizadeh H, Dariushi S, Salami SJ. Optimal face sheet thickness of 3D printed polymeric hexagonal and re-entrant honeycomb sandwich beams subjected to three-point bending. Compos Struct 2022;291:115618.
[27] Safaei B, Onyibo EC, Hurdoganoglu D. Effect of static and harmonic loading on the honeycomb sandwich beam by using finite element method. Facta Universitatis-Series Mech Eng 2022;20:279–306.
[28] Daikh AA, Belarbi MO, Ahmed D, Houari MSA, Avcar M, Tounsi A, et al. Static analysis of functionally graded plate structures resting on variable elastic foundation under various boundary conditions. Acta Mech 2023;234:775–806.
[29] Zhang XG, Jiang W, Zhang Y, Luo C, Zhang XY, Han D, et al. Energy absorption properties of composite tubes with hexagonal and re-entrant honeycomb fillers. Constr Build Mater 2022;356:129298.
[30] Xia FK, Durandet Y, Tan P, Ruan D. Three-point bending performance of sandwich panels with various types of cores. Thin-Walled Struct 2022;179:109723.
[31] Garg A, Belarbi MO, Chalak HD, Li L, Sharma A, Avcar M, et al. Buckling and free vibration analysis of bio-inspired laminated sandwich plates with helicoidal/Bouligand face sheets containing softcore. Ocean Eng 2023;270:113684.
[32] Gunaydin K, Rea C, Kazanci Z. Energy absorption enhancement of additively manufactured hexagonal and re-entrant (auxetic) lattice structures by using multi-material reinforcements. Addit Manuf 2022;59:103076.
[33] Ha NS, Pham TM, Tran TT, Hao H, Lu GX. Mechanical properties and energy absorption of bio-inspired hierarchical circular honeycomb. Compos Part B 2022;236:109818.
[34] Teng XC, Ren X, Zhang Y, Jiang W, Pan Y, Zhang XG, et al. A simple 3D re-entrant auxetic metamaterial with enhanced energy absorption. Int J Mech Sci 2022;229:107524.
[35] Hamzehei R, Zolfagharian A, Dariushi S, Bodaghi M. 3D-printed bio-inspired zero Poisson's ratio graded metamaterials with high energy absorption performance. Smart Mater Struct 2022;31:035001.
[36] Xu SQ, Beynon JH, Ruan D, Lu GX. Experimental study of the out-of-plane dynamic compression of hexagonal honeycombs. Compos Struct 2012;94:2326–36.
[37] Meng ZQ, Ouyang Z, Chen CQ. Multi-step metamaterials with two phases of elastic and plastic deformation. Compos Struct 2021;271:114152.
[38] Wu X, Su YT, Shi J. In-plane impact resistance enhancement with a graded cell-wall angle design for auxetic metamaterials. Compos Struct 2020;247:112451.
[39] Usta F, Turkmen HS, Scarpa F. High-velocity impact resistance of doubly curved sandwich panels with re-entrant honeycomb and foam core. Int J Impact Eng 2022;165:104230.
[40] Andrew JJ, Schneider J, Schiffer A, Hafeez F, Kumar S. Dynamic crushing of tailored honeycombs realized via additive manufacturing. Int J Mech Sci 2022;219:107126.
[41] Liang HY, Hao WQ, Xue GL, Liu BC, Pu YF, Ma FW. Parametric design strategy of a novel self-similar hierarchical honeycomb for multi-stage energy absorption demand. Int J Mech Sci 2022;217:107029.
[42] Zhang XC, Dong SJ, An CC, Wu HX, Niu XY. Dynamic crushing behaviors of multi-Layered gradient honeycombs with different Poisson's ratios: a finite element simulation. Int J Appl Mech 2022;14:2150127.
[43] Fu MH, Liu FM, Hu LL. A novel category of 3D chiral material with negative Poisson's ratio. Compos Sci Technol 2018;160:111–8.
[44] Shukla S, Behera BK. Auxetic fibrous structures and their composites: a review. Compos Struct 2022;290:115530.
[45] Liu K, Cao XF, Zhang P, Wu WW, Li Y. Dynamic mechanical performances of enhanced anti-tetra-chiral structure with rolled cross-section ligaments under impact loading. Int J Impact Eng 2022;166:104204.
[46] Bodaghi M, Serjouei A, Zolfagharian A, Fotouhi M, Rahman H, Durand D. Reversible energy absorbing meta-sandwiches by FDM 4D printing. Int J Mech Sci 2020;173:105451.
[47] Han D, Ren X, Luo C, Zhang Y, Zhang XY, Zhang XG, et al. Experimental and computational investigations of novel 3D printed square tubular lattice metamaterials with negative Poisson's ratio. Addit Manuf 2022;55:102789.
[48] Jiang F, Yang S, Ding C, Qi C. Quasi-static crushing behavior of novel circular double arrowed auxetic honeycombs: experimental test and numerical simulation. Thin-Walled Struct 2022;177:109434.
[49] Del Broccolo S, Laurenzi S, Scarpa F. AUXHEX - A Kirigami inspired zero Poisson's ratio cellular structure. Compos Struct 2017;176:433–41.
[50] Ingrole A, Hao A, Liang R. Design and modeling of auxetic and hybrid honeycomb structures for in-plane property enhancement. Mater Des 2017;117:72–83.
[51] Farrokhabadi A, Ashrafian MM, Behravesh AH, Hedayati SK. Assessment of fiber-reinforcement and foam-filling in the directional energy absorption performance of a 3D printed accordion cellular structure. Compos Struct 2022;297:115945.
[52] Qin Q, Dayyani I, Webb P. Structural Mechanics of cylindrical fish-cell zero Poisson's ratio metamaterials. Compos Struct 2022;289:115455.
[53] Zhu HY, Fan HL. Manufacturing and testing of CFRC sandwich cylinder with zero Poisson's ratio Kevlar meta-honeycomb core layer. Compos Sci Technol 2022;230:109774.
[54] Sahariah BJ, Baishya MJ, Namdeo A, Khanikar P. A novel strategy to design lattice structures with zero Poisson's ratio. Eng Struct 2023;288:116214.

[55] Yang H, Leow WR, Wang T, Wang J, Yu JC, He K, et al. 3D printed photo responsive devices based on shape memory composites. Adv Mater 2017;29: 1701627.
[56] Yu R, Yang X, Zhang Y, Zhao XJ, Wu X, Zhao TT, et al. Three-dimensional printing of shape memory composites with epoxy-acrylate hybrid photopolymer. ACS Appl Mater Interfaces 2017;9:1820–9.
[57] Ren HL, Yang XD, Wang ZH, Xu XG, Wang R, Ge Q, et al. Smart structures with embedded flexible sensors fabricated by fused deposition modeling-based multimaterial 3D printing. Int J Smart Nano Mater 2022;13:447–64.
[58] Arif ZU, Khalid MY, Noroozi R, Sadeghianmaryan A, Jalalvand M, Hossain M. Recent advances in 3D-printed polylactide and polycaprolactone-based biomaterials for tissue engineering applications. Int J Biol Macromol 2022;218: 930–68.
[59] Zhao YL, Liu F, Zhu KJ, Maganti S, Zhao ZY, Bai PK. Three-dimensional printing of the copper sulfate hybrid composites for supercapacitor electrodes with ultra-high areal and volumetric capacitances. Adv Compos Hybrid Mater 2022;5:1537–47.
[60] Chen DB, Liu QP, Han ZW, Zhang JQ, Song HL, Wang KJ, et al. 4D printing strain self-sensing and temperature self-sensing integrated sensor-actuator with bioinspired gradient gaps. Adv Sci 2020;7:2000584.
[61] Yousuf MH, Abuzaid W, Alkhader M. 4D printed auxetic structures with tunable mechanical properties. Addit Manuf 2020;35:101364.
[62] Zhao W, Huang ZP, Liu LW, Wang WB, Leng JS, Liu YJ. Porous bone tissue scaffold concept based on shape memory PLA/Fe_3O_4. Compos Sci Technol 2021;203: 108563.
[63] Ding AX, Jeon O, Cleveland D, Gasvoda KL, Wells D, Lee SJ, et al. Jammed micro-flake hydrogel for four-dimensional living cell bioprinting. Adv Mater 2022;34: 2109394.
[64] Siminska-Stanny J, Niziol M, Szymczyk-Ziolkowska P, Brozyna M, Junka A, Shavandi A, et al. 4D printing of patterned multimaterial magnetic hydrogel actuators. Addit Manuf 2022;49:102506.
[65] Chen X, Han SY, Wu WH, Wu ZH, Yuan Y, Wu J, et al. Harnessing 4D printing bioscaffolds for advanced orthopedics. Small 2022;18:2106824.
[66] Ding AX, Lee SJ, Ayyagari S, Tang R, Huynh CT, Alsberg E. 4D biofabrication via instantly generated graded hydrogel scaffolds. Bioact Mater 2022;7:324–32.
[67] Wan X, He Y, Liu YJ, Leng JS. 4D printing of multiple shape memory polymer and nanocomposites with biocompatible, programmable and selectively actuated properties. Addit Manuf 2022;53:102689.
[68] Ly ST, Kim JY. 4D printing - fused deposition modeling printing with thermal-responsive shape memory polymers. Int J Precis Eng Manufacturing-Green Technol 2017;4:267–72.
[69] Liu H, Wang FF, Wu WY, Dong XF, Sang L. 4D printing of mechanically robust PLA/TPU/Fe_3O_4 magneto-responsive shape memory polymers for smart structures. Compos Part B 2023;248:110382.
[70] Zhang JF, Yin ZF, Ren LQ, Liu QP, Ren L, Yang X, et al. Advances in 4D printed shape memory polymers: from 3D printing, smart excitation, and response to applications. Adv Mater Technol 2022;7:2101568.
[71] Zhao W, Li N, Liu LW, Leng JS, Liu YJ. Origami derived self-assembly stents fabricated via 4D printing. Compos Struct 2022;293:115669.
[72] Zhang FH, Wen N, Wang LL, Bai YQ, Leng JS. Design of 4D printed shape-changing tracheal stent and remote controlling actuation. Int J Smart Nano Mater 2021;12: 375–89.
[73] Zolfagharian A, Durran L, Gharaie S, Rolfe B, Kaynak A, Bodaghi M. 4D printing soft robots guided by machine learning and finite element models. Sens Actuators A 2021;328:112774.
[74] Skarsetz O, Slesarenko V, Walther A. Programmable auxeticity in hydrogel metamaterials via shape-morphing unit cells. Adv Sci 2022;9:2201867.
[75] Ren LQ, Wu Q, Liu QP, Hao PT, Tang JH, Li JY, et al. Stiffness-tunable and self-sensing integrated soft machines based on 4D printed conductive shape memory composites. Mater Des 2023;228:111851.
[76] Xin XZ, Liu LW, Liu YJ, Leng JS. 4D Printing auxetic metamaterials with tunable, programmable, and reconfigurable mechanical properties. Adv Funct Mater 2020; 30:2004226.
[77] Liu H, Liu RA, Chen K, Liu YY, Zhao Y, Cui XY, et al. Bioinspired gradient structured soft actuators: from fabrication to application. Chem Eng J 2023;461: 141966.
[78] Zolfagharian A, Bodaghi M, Hamzehei R, Parr L, Fard M, Rolfe BF. 3D-printed programmable mechanical metamaterials for vibration isolation and buckling control. Sustainability 2022;14:8631.
[79] Wu LL, Wang Y, Zhai ZR, Yang Y, Krishnaraju D, Lu JQ, et al. Mechanical metamaterials for full-band mechanical wave shielding. Appl Mater Today 2020; 20:100671.
[80] Zheng YS, Zhang XN, Luo YJ, Yan B, Ma CC. Design and experiment of a high-static-low-dynamic stiffness isolator using a negative stiffness magnetic spring. J Sound Vib 2016;360:31–52.
[81] Olympio KR, Gandhi F. Zero Poisson's ratio cellular honeycombs for flex skins undergoing one-dimensional morphing. J Intell Mater Syst Struct 2010;21: 1737–53.
[82] Zhang W, Zhang FH, Lan X, Leng JS, Wu AS, Bryson TM, et al. Shape memory behavior and recovery force of 4D printed textile functional composites. Compos Sci Technol 2018;160:224–30.
[83] Ju J, Kim DM, Kim K. Flexible cellular solid spokes of a non-pneumatic tire. Compos Struct 2012;94:2285–95.
[84] Zolfagharian A, Picken P, Bodaghi M, Fard M, Rolf B. Additive manufacturing of composite foam metamaterial springs for vibration isolation. Adv Eng Mater 2023: 2300356. https://doi.org/10.1002/adem.202300356.